UTRECHT UNIVERSITY

MASTER THESIS

Hierarchical self-assembly of surfactant/polysaccharide complexes studied by small angle X-ray scattering

---

Author:
Tatiana Komarova

Supervision by:
Dr. Andrei Petukhov
Dr. Jasper Landman
Dr. Theyencheri Narayanan

Van 't Hoff Laboratory for Physical and Colloid Chemistry
Debye Institute for Nanomaterials Science

June 29, 2022

Abstract

Aqueous solutions of β-cyclodextrin (β-CD) and sodium dodecyl sulfate (SDS) are known to spontaneously form concentration-dependent assemblies with complex multiscale structure. In particular, supramolecular multilayered tubular aggregates exhibit striking morphological similarities with peptide nanotubes, bacterial protein shells, or multiwalled carbon nanotubes that hint at the existence of some similarities in their formation mechanism. Since the spatial scales involved in this mechanism range from about a nanometer (the size of SDS@2β-CD complexes) through a micron (microtube diameter), small-angle X-ray scattering (SAXS) is an ideal experimental technique that allows one to track changes in the structural organization on different length scales. According to the results of recent SAXS experiments, temperature-induced microtube assembly/disassembly follows the inward growth mechanism proposed earlier. The outermost tube radius is highly sensitive to the temperature, while SDS@2β-CD complex concentration insignificantly affects this quantity. As temperature increases towards the melting point, the number of walls inside a microtube decreases, and the microtube swells. As a result of the interplay between the bending energy and bond formation, the temperature dependence of the outermost radius of microtubes sheds light on the energetics of the self-assembly, allowing us to estimate the energies of H-bonds involved in this process. On the contrary, the system demonstrates a different, two-level response to the applied moderate hydrostatic pressure (100-200 bar). The first, fast process (~0.3 s) involves the shrinking of microtubes without any significant changes in the number of cylinders inside or the distance between them. In the second slower process (~tens s), inner layers of microtubes disintegrate as less energetically favourable. Opposite to the temperature static studies, this disassembly process is irreversible. After pressure is released, the structure does not return to the initial state presumably being stuck in a local minimum on the energy landscape.

Contents

iv

Chapter 1

Introduction

1.1 Self-assembled crystalline superstructures

For many years the birth of order out of chaos has been fascinating scientists and encouraging them to uncover its secrets. On time scales sufficient for a colloidal system (particles with a size between a nanometer and a micrometer dispersed in a solvent) to explore a given space through a random motion, its components can spontaneously and reversibly form an organized structure. This process holds a name *self-assembly*: building units of a self-organized aggregate either do not interact with each other (hard-sphere colloids at high volume fractions [1]) or form non-covalent bonding (Van der Waals forces, electrostatic interactions, hydrophobic effect, π-interactions). Among scientific goals related to self-assembly is not only studying its underlying mechanisms, but also searching for general principles applicable to describe behavior of various systems, including those existing in nature.

In particular, protein self-assembly into crystalline superstructures has been attracting researchers' attention for a long time [2–4]. To better understand processes behind it, scientists have been searching and analyzing synthetic systems that follow similar self-assembly patterns. Cyclic oligosaccharides (cyclodextrins) - amphiphilic molecules consisting from both hydrophilic and hydrophobic parts that are known to produce plenty of supramolecular aggregates when mixed with various surfactants [5–7]. Recently, Yang *et al.* [8] reported lamellae, tubes, and rhombic dodecahedra based on a rigid crystalline membrane formed in solutions of β-cyclodextrin and anionic surfactant sodium dodecyl sulfate. They also demonstrated striking similarities between the formed superstructures and protein- and peptide-based aggregates.

1.2 SDS@2β-CD tubular aggregates

Hierarchical self-assembly of β-cyclodextrin and sodium dodecyl sulfate starts from inclusion complexes with the 2:1 (β-CD:SDS) stoichiometry, Figure 1.1A. The complex formation is driven by the hydrophobic effect: trying to minimize its contact with water, a hydrophobic SDS tail goes into a channel formed by two β-CD molecules [1]. Then, hydrophobic interactions and hydrogen bonding force complexes to form bi-complexes (Figure 1.1B-C) which are being self-assembled into negatively charged (determined by the charge of the SDS head group) crystalline membranes held by the H-bonds between β-CD molecules. In a plane (Figure 1.1D), the bilayer

---

[1]The complex stoichiometry varies based on the length of the surfactant alkyl chain and the size of the cyclodextrin interior. For example, γ-cyclodextrin which has a larger cavity (0.75-0.83 nm in diameter against 0.6-0.65 nm of β-CD) is able to accommodate two alkyl chains per sugar molecule [10].
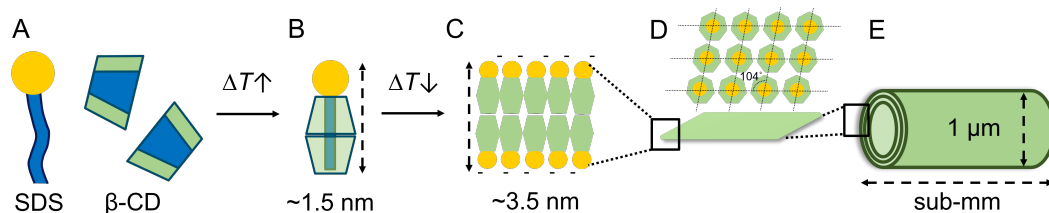
Figure 1.1: Sodium dodecyl sulfate and β-cyclodextrin self-assembly into multiwalled microtubes. (A) An aqueous solution containing SDS and β-CD in 1:2 molar ratio is heated up to 60°C. (B) A hydrophobic tail of an SDS molecule and a hydrophobic cavity of β-CD minimize their interaction with water by forming SDS@2β-CD complexes. (C) The resulted structural units are still hydrophobic at the bottom so they assemble into negatively charged bilayers (the charge is determined by the SDS head group). (D) Since β-CD molecules are prone to form inter-hydrogen bonding, bilayers are constructed into two-dimentional crystalline membranes with a rhombic 2D unit cell. (E) If membranes are large enough so the bonding energy gained after the cylindrical closure exceeds their bending energy, they are rolled up into multiwalled microtubes [9]. The distance between inner cylinders inside a tube is defined by the competition between the bending energy of wrapped bilayer sheets and electrostatic repulsion between them [9].

sheet is organized as a rhombic lattice: a unit cell length - 1.52 nm, an obtuse angle - 104°. The rhombic lattice was found to be related with the 7-fold symmetry of the β-CD molecule [8]. The angle of 104° ensures maximum inter-cyclodextrin hydrogen bonding within the sheet plane. Depending on the concentration in the solution, these bilayer sheets can thermoreversibly turn either into vesicles, or into multiwalled microtubes, or into lamellae [8].

The following thesis is focusing on the structural characterization of tubular aggregates, Figure 1.1E. The formed tubular phase is extremely attractive for both practical use (e.g. controlled drug release [11] or 1D artificial colloid confinement [12, 13]) and for fundamental research from the perspective on the hierarchical self-assembly [14]. The proposed potential applications require profound knowledge about the microtube structure. We are interested in temperature- and concentration-dependent sensitivity of the microtube geometrical parameters (diameter, number of walls inside a tube, distance between them); transition point of the temperature-induced microtube assembly/disassembly; influence of the applied pressure; *etc*.

1.3 SAXS for microtube characterization

Small-angle X-ray scattering is a suitable method for studying the structure of nanomaterials and soft matter in bulk [16, 17]. After irradiation of the sample with X-rays, its scattering pattern is being recorded. The scattering of the sample occurs due to the existence of a scattering contrast between objects in the solution. The scattering contrast results from spatial modulations of the electron density, varying depending on the number of electrons in the atoms of the constituent elements. The contrast is represented by the difference in the scattering length density (SLD) of the objects of interest and their environment [18]. For sufficiently diluted samples, SAXS can feature the average size of scatterers, their polydispersity, shape, morphology, and how the electron density is distributed inside the scattering objects [19].

A schematic of a typical SAXS experiment geometry is shown in Figure 1.2. First,
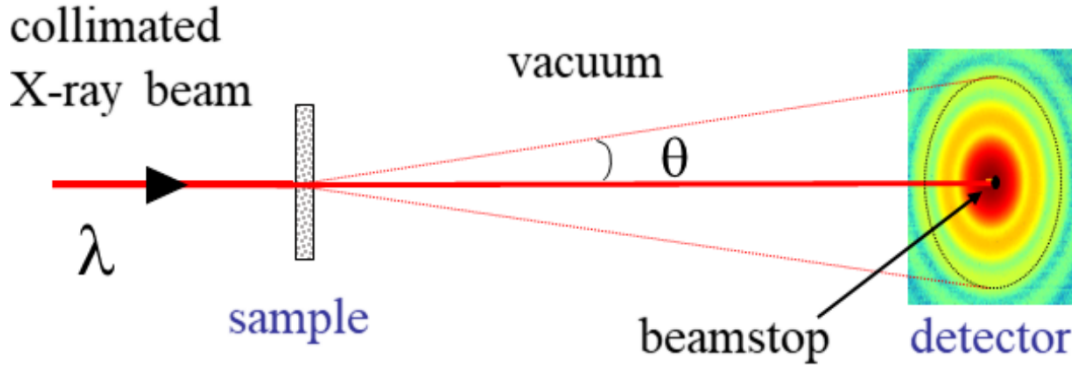
Figure 1.2: Schematic of a SAXS experiment including crucial components. The original X-ray beam is split to the scattered and transmitted beams after interacting with a sample. The transmitted beam is blocked by a beam stop; the scattered beam deflected by an angle θ is detected by a 2D detector. The picture is taken from [15].

an incident X-ray beam is being monochromated (after this procedure it can be characterized with a photon-energy dependent wavelength λ) and collimated with a special optical setup. Second, this beam interacts with a sample and the forwardly scattered intensity is being recorded by a 2D detector. The 2D detector essentially counts the number of photons dependent of a scattering angle θ.

In addition to the scattering process, the sample-beam interaction includes the transmission of the incident beam, which is blocked by a beamstop without reaching the detector. To avoid air absorption and scattering, X-rays propagate in vacuum before and after the sample, while the sample is in ambient conditions [15].

Considering fully elastic scattering at small angles, the incident ($\mathbf{k_i}$) and scattered ($\mathbf{k_s}$) wave vectors are assumed to be of equal amplitudes ($\frac{2\pi}{\lambda}$). The scattering vector is their difference $\mathbf{q} = \mathbf{k_s} - \mathbf{k_i}$ with the length depending on the scattering angle θ and the X-ray wavelength λ:

$$q = \frac{4\pi}{\lambda}\sin\left(\frac{\theta}{2}\right). \tag{1.1}$$

Length scales measured in scattering experiments are approximately $\frac{2\pi}{q}$. Different length scales are probed in the scattering experiment by changing the sample-detector distance (this change the available θ range) with a given λ. The scattered intensity has units m^{-1} sr^{-1}: reverse length times reverse steradian. It is defined as the number of photons scattered per unit solid angle of the detector divided by the sample thickness, the total amount of photons, the sample transmittance and detector efficiency. This quantity contains information on the structure of scatteres (*form factor*) and their interactions (*structure factor*) in the illuminated volume over the q-range available in the SAXS experiment.

The resolution of the conventional SAXS technique is insufficient to characterize objects whose structural features are about hundreds of nanometers. This can be surpassed by using more advanced high-resolution optics. The resulting experimental setup holds a name *ultra small-angle X-ray scattering*, USAXS and allows one to measure much smaller angles [20]. Thanks to recent advances in SAXS instrumentation, using USAXS enables achieving lengths up to a micrometer and higher [18].

To get the structural information on the sample at smaller length scales, wide

scattering angles are needed. They can be obtained using the wide-angle X-ray scattering technique or WAXS. The total range of nominal length scales that can be observed in the scattering experiment using USAXS, SAXS and WAXS is demonstrated in Figure 1.3: the overlap between different scattering techniques is not strict and depends on the interpretation. Besides the length scales, comprehensive time scales (6 orders) accessible for analysis during synchrotron scattering experiments are also shown.
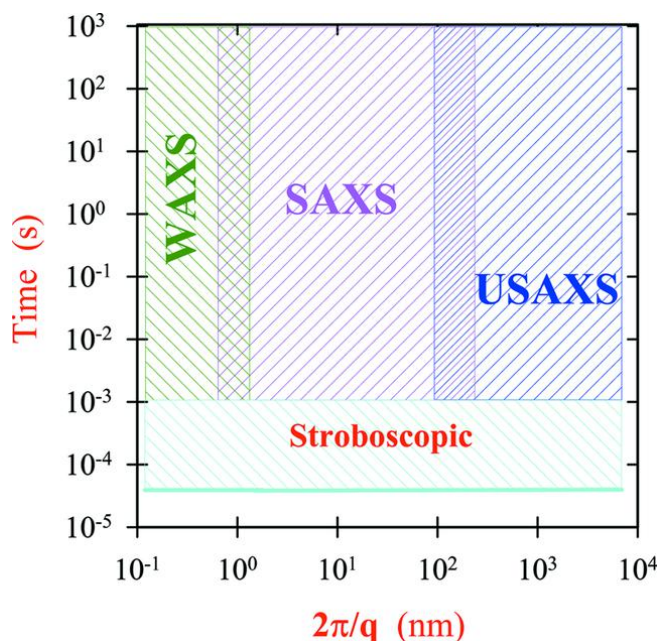
Figure 1.3: Nominal length $\frac{2\pi}{q}$ and timescales accessible by USAXS, SAXS and WAXS techniques for a sample having sufficient structural features over the spanned range. The scheme is taken from [21].

SAXS is a method allowing for *in situ* structural characterization of a sample. It does not require tedious sample preparation that can damage a specimen (electron microscopy experiments [22, 23]). Thus, it is an ideal experimental technique to study SDS@2β-CD supramolecular aggregates covering spatial scales in the range from about a nanometer (size of SDS@2β-CD complexes) through a micron (microtube diameter). In particular, Ouhaji *et al.* first demonstrated in their study a SAXS pattern of SDS@2β-CD microtubes with structural features spanning reciprocal length scales from 0.0015 nm^{-1} to 8 nm^{-1} [24]. Figure 1.4 displays in detail the power of the scattering experiment to study the microtube hierarchy. One is able to track down three regions corresponding to the in-plane complex organization (Figure 1.4B), organization of inner layers inside a tube (Figure 1.4C), the average tube cross-section size (Figure 1.4D).
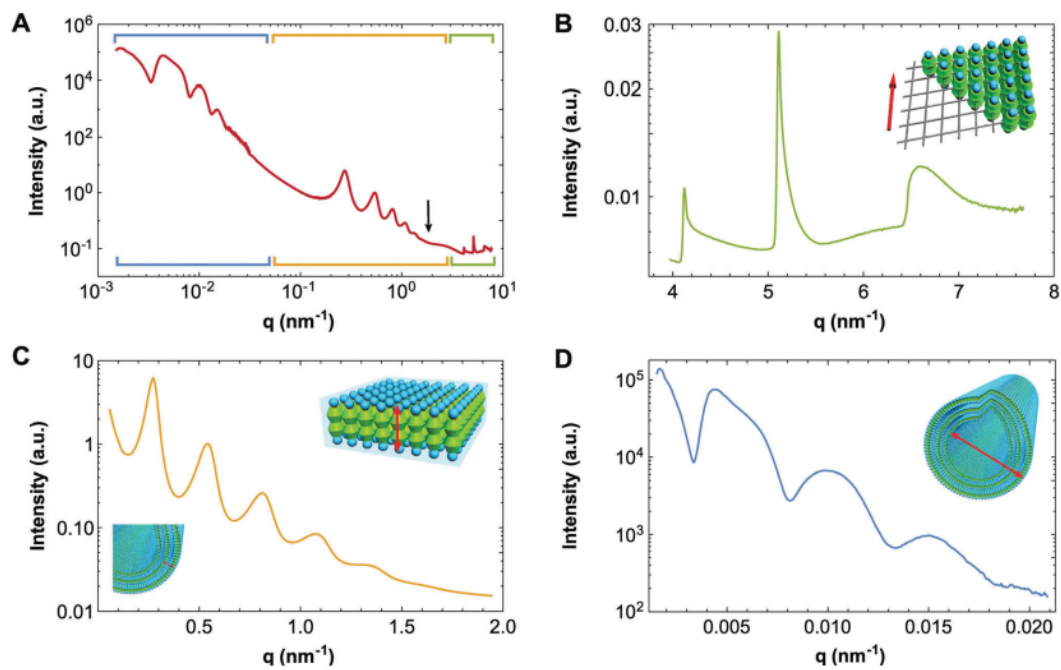
Figure 1.4: Three main regions revealing different microtube features at the SAXS experiment where the 10 wt% was loaded in the capillary. (A) Radial intensity profile I as a function of wavevector q showing the complete set of data, measured using three sample-to-detector distances. The black arrow pinpoints the form factor minimum of the bilayers. (B) The saw-tooth shaped peak characteristic of 2D structures at high q. The inset shows the in-plane rhombic unit cell. (C) Inter- and intra-bilayer structure of the walls of the microtubes with a lamellar spacing of 23 nm. Insets show models of the bilayer and the multiwalled structure of the microtubes. The red arrows illustrate the bilayer thickness and interlamella distance. (D) At low q, the average diameter of the microtubes can be observed as indicated with the red arrow in the inset. The picture and its caption are taken from [24].

Chapter 2

Experimental section

2.1 Preparation of microtube suspensions

β-CD (Sigma-Aldrich, 97%), SDS (Sigma-Aldrich, > 99%) and Milli-Q water were weighed and mixed together in the desired amounts with a constant SDS to the β-CD 1:2 molar ratio. SDS was used to prepare samples as received. β-CD was dried to get rid of water as it is known for its hygroscopicity [25]. According to the gravimetric analysis of the β-CD powder before/after dehydration (drying oven, $120°C$, 24 hours), there were 11 H_2O molecules per one sugar molecule. A sample series with SDS@2β-CD concentrations ranging from 3 weight % (wt%) to 20 wt% was prepared. Mixtures were stirred and heated up to $70°C$, until a turbid solution has changed to a transparent one corresponding to the SDS@2β-CD complex emergence. Then, hot solutions were kept for 48 hours at room temperature for tubular phase formation yielding turbid, viscous gels. Dynamics of the turbidity appearance depends on the concentration: the higher the concentration, the faster the sample becomes turbid and highly viscous. For samples with extremely high concentrations (30, 40 wt%), the turbidity is less pronounced, which supposedly results from the formations of another, lamellar phase (Figure 2.1).
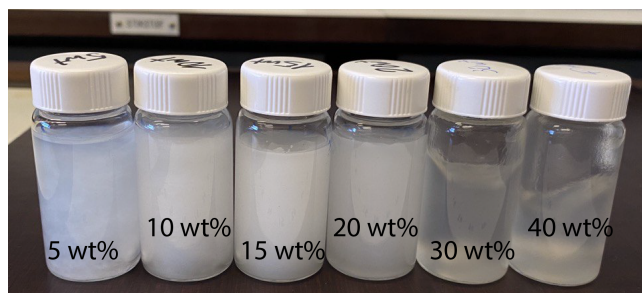
Figure 2.1: A sample series of different concentrations that has been equilibrated for a week under normal conditions. A turbid, watery sample with 5 wt% is around its transition point at room temperature. Samples of higher concentrations (10-30 wt%) are whitish, viscous and turbid while samples of 30-40wt% are extremely viscous but almost transparent.

2.2 Small-angle X-ray scattering

Scattering data were recorded using a Eiger2 4M (Dectris AG) hybrid pixel-array detector with tunable sample-to-detector distances: from 31 m for small angles (q_0 = 0.0025 nm^{-1}) to 1 m for larger angles (q_1 = 8 nm^{-1}). These distances allow one to cover nominal sizes from 0.8 nm to 2.4 μm. The detector records a 2D scattering pattern of a sample. Data reduction (azimuthal averaging) was carried out for 2D

isotropic scattering patterns. The background correction was performed for all 1D radial profiles or 2D patterns shown in the thesis text. Subtracted background was a scattering curve recorded at the same conditions as samples from a capillary with a Milli-Q water. The X-ray wavelength used in all experiments was $\lambda = 0.1$ nm.

Since it is impossible to cover length scales featuring both radius oscillations and crystalline structure in one scattering experiment, the sample-to-detector distance has to be changed after the experiment is finished. Then, the scattering experiment is repeated under the same conditions with a sample from the same vial, which was not modified during the first experiment. That provides identical conditions for all taken scattering curves. Then, the recorded curves are merged to span all nominal length scales of interest.

All scattering experiments, the results of which are considered in this thesis, have been performed at ID02 beamline, European Synchrotron Radiation Facility (ESRF) employing different sample environments enlisted below.

2.2.1 Heating stage

Samples with different concentrations (in the range from 3 wt% to 20 wt%) were loaded into quartz capillaries with a diameter of 2 mm. Capillaries were sealed to prevent the solvent evaporation. Since the studied samples are viscous, the shear effect resulting from capillary filling affects the scattering patterns. 2D scattering images are slightly oriented, which makes subsequent data reduction somewhat troublesome. To avoid this, all sealed capillaries were heated to a temperature at which all structural features corresponding to the tubular phase disappear (60°C) before the experiments. This procedure ensured that the samples were brought to the same molten state. Then, solutions consisting of single complexes were gradually cooled down with a cooling rate 0.2°C/min and left for ten minutes at a set temperature to achieve equilibrium before recording the SAXS pattern. A downramp series was recorded in the temperature range of 60°C-10°C with a step of 1°C. Afterwards, a temperature upramp series was recorded following the same parameters covering 10°C-60°C temperature range.

2.2.2 Pressure jump

A sample with 6.5 wt% concentration (50 µl) was loaded in a polycarbonate cell (Figure 2.2A) and then quickly compressed (up to 1 kbar in less than 1 ms) [26]. The high-pressure setup is based on a high force piezo stack (Figure 2.2B) allowing for rapid dynamically compression; temperature control was also available. The pressure chamber windows are made of polished diamond, providing the cell stability within a few kilobars. The pressure values that were used in the scattering experiments did not exceed 250 bar.

After the pressure was increased, the X-ray beam penetrated the sample through the diamond windows. 2D scattering patterns were recorded with a chosen time interval to detect the sample changes after the jump.

2.2.3 Couette cell coupled with the stress controlled rheometer

A sample with 6.5 wt% concentration (≈ 50 µl) was loaded in a coaxial capillary Couette cell: the space between two cylinders where the inner one rotates and the outer one does not move. The shaft of the stress controlled rheometer drives the X-ray transparent cell with a controllable shear rate up to 250 s^{-1} ensuring the sample
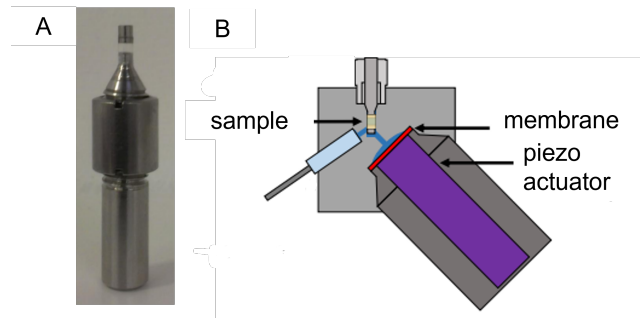
Figure 2.2: Schematic of the pressure cell and sample container. The image was taken from [26] and adapted. A) A sample holder combined with a polycarbonate capillary (to be filled with a sample) and a closing plug. The plug has to tightly seal the cell to avoid sample leaking. B) Sketch of the presurre cell cross-section where the sample holder is mounted from the top, the pressure tranducer and the piezo-actuator with the flexible membrane (red colored) mounted from other sides.

orientation. The incident X-ray beam enters the cell through the spotted window on the enclosure. The SAXS patterns can be registered in velocity/vorticity and shear/vorticity planes using this microvolume shear cell. Temperature control eliminates the heating effects caused by the shear [27].

2.3   Imaging: polarized light microscopy (PLM)

To study melting behavior of tubular aggregates, the prepared suspension was loaded into a rectangular glass capillary (Vitrocom, $0.1 \times 2 \times 50$ mm), sealed by an ultraviolet-curing epoxy glue. Nikon Eclipse E400 POL polarising microscope equipped with Linkam heating stage was used to conduct experiments in the polarization mode to track the presence of birefringence in the sample at various temperatures.

PLM uses polarized light for the sample illumination. The incident non-polarized light first goes through a polarizer that cuts off all orientations except for one. Then, the resulting linearly polarized light, which electric vector oscillates only in one direction, meets a sample. If the sample is birefringent (there are two refractive indices in the sample), it interacts with the light in a special way. Particularly, the outcoming light-wave is split into ordinary and extraordinary rays that propagate within the sample with different speeds because of different refractive indices. These two rays go to an analyzer (essentially the second polarizer). The analyzer allows for passing only light waves with an electric vector perpendicular to the linearly polarized light created by the polarizer. These optical elements together allow one to detect and measure the retardation between ordinary and extraordinary waves occurring in the birefringent sample.

Colors that are produced in the PLM depend on the type of the sample, its thickness and orientation on the specimen slide. Usually the optical contrast (Δn) is tiny, so the PLM images are not colorful. To determine the birefringence sign and enhance the optical contrast, retarders or waveplates are introduced before the analyzer. To produce PLM images presented below, a full-wave plate was installed in the polarizing microscope during the experiments.

2.4   Analysis

The visualization of the obtained SAXS experiment results was accomplished using the software *SaxsUtilities* [28] and Python scripts. The fitting procedure 1D SAXS curves was also performed using custom Python scripts, the software *Sasview*.

Chapter 3

Results and discussion

3.1 Sample alignment *via* shear cell

The idea behind this thesis was to study the internal structure of the microtube. As it was shown in Chapter 1, the SAXS technique is a powerful experimental approach for that. To extract quantitative information from the SAXS curves, it is necessary to find a suitable model to describe the experimental data. In this section, we use shear alignment of the sample to check whether the multiwalled structure refers only to the tubular phase.

Shear stress is known to influence soft matter materials. The shear flow aligns anisotropic objects in the desired direction. To study whether the multilayered structure observed in Figure 1.4C is characteristic for the tubular phase but not to the lamellar stacking of flat bilayer sheets, sample shear alignment was combined with small-angle X-ray scattering. This approach significantly increases the information content in the recorded 2D oriented scattering patterns [27].
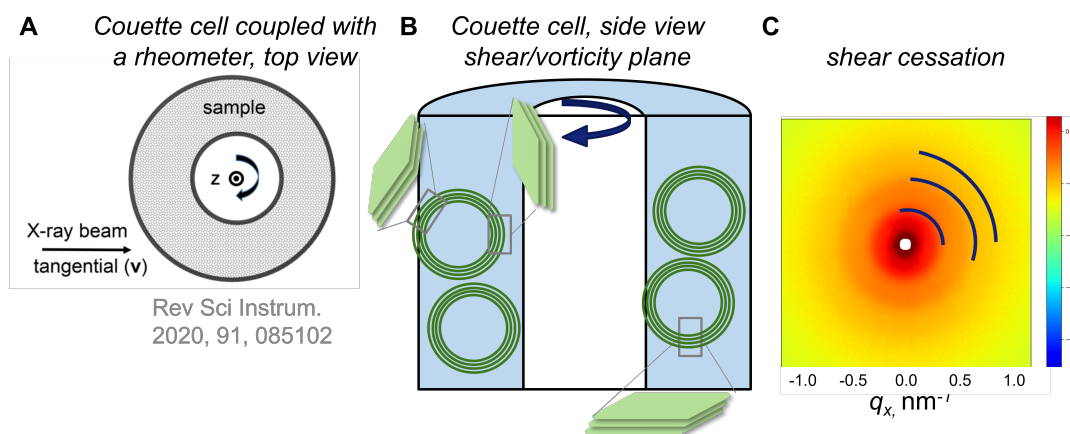
Figure 3.1: Schematic view of two concentric capillaries from the top, along with a tangential X-ray beam position and results of such an experiment. B) The schematic of microtubes aligned in the shear-vorticity plane: here the main axis of microtubes is perpendicular to the considered plane. Therefore, scattering from the microtube cross-section is recorded. C) 2D scattering pattern taken in the considered direction using 1m sample-to-detector distance: the pattern is isotropic as lamellar stacking is correlated with microtube cross-section (all lamellae orientations are present). Dark arcs correspond to the pseudo-Bragg peaks of different orders.
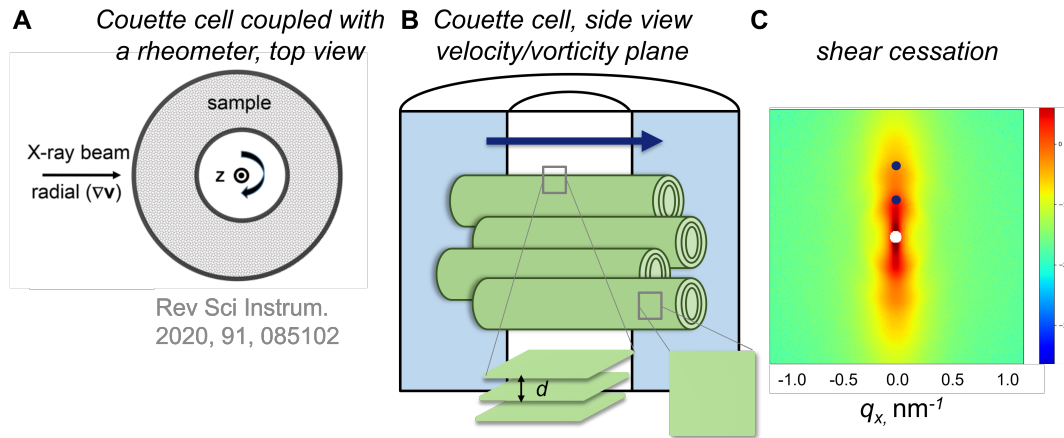
During the experiment, 2D SAXS patterns from a sample of 6.5 wt% were recorded in shear/vorticity (Figure 3.1) and velocity/vorticity (Figure 3.2) planes of the coaxial capillary shear cell immediately after shear cessation. The sample-to-detector distance was about 1 m to cover the region of pseudo-Bragg peaks appearing in Figure 1.4C.

First, let us take a look on the shear/vorticity plane. In Figure 3.1C, a fully isotropic 2D scattering pattern is shown. Guided by the shear flow (Figure 3.1A), the main axis of a tube is perpendicular to the considered plane. Multilamellar microtube cross-section (Figure 3.1B) consists of concentric cylinders: lamellar stacking is presented at all possible orientations, therefore, the recorded pattern is isotropic. The dark arcs in Figure 3.1C represent pseudo-Bragg peaks of different order (Equation 3.1). If layered stacking comes from flat sheets, its presence can be noticed on the velocity/vorticity plane.

$$2d\sin\theta = n\lambda, \tag{3.1}$$

Here λ is the radiation wavelength, θ - glancing angle, $\langle d \rangle$ - interbilayer separation between microtube inner layers.

Another possibility in the experiment with the sample alignment is to look at the velocity/vorticity plane. In Figure 3.2, the 2D pattern from the velocity/vorticity plane of the shear aligned sample is demonstrated. Tubes are aligned along the shear flow, therefore, the scattering pattern in the considered plane is vertically oriented. The orientation of bilayers that can appear in the scattering pattern is shown in Figure 3.2B. Only vertical stacking (bilayer sheets lie on top of each other) can contribute to the sample scattering. Discrete-like maxima of scattered intensity (dark points in Figure 3.2C) correspond to the different diffraction orders (n) in Bragg's Law (Equation 3.1).

A *Couette cell coupled with a rheometer, top view* **B** *Couette cell, side view velocity/vorticity plane* **C** *shear cessation*

Rev Sci Instrum. 2020, 91, 085102

Figure 3.2: Schematic view of two concentric capillaries from the top, along with a radial beam position and results of such an experiment. The internal cylinder is rotating while the outer cylinder stays still. The space between the cylinders is filled with a sample. (A) The vorticity ($\vec{z}$) is along the axis of the cylinders, radial position is along the flow velocity ($\vec{v}$) direction. The arrow shows the direction of the initial X-ray beam that goes through the setup. (B) In the velocity-vorticity plane, microtubes are aligned horizontally as their main axis follows the flow direction. Therefore, only specific orientations of lamellar stacking (zoomed in the figure) can be seen in a 2D scattering pattern. d is the interbilayer separation in Equation 3.1. (C) 2D scattering pattern taken in the considered direction using 1 m sample-to-detector distance: the pattern is anisotropic as microtubes are horizontally aligned.

Such an experiment allows us to draw conclusions about structures floating in the solution. In the considered case, the lamellar phase detected during the scattering experiment can only be attributed to microtubes. If lamellar stacking was formed by flat bilayer sheets, the two-dimensional pattern in the shear-vorticity plane would be (partially) oriented. The conclusions drawn on the basis of the above described

experiments will allow us to freely use concentric cylinders form factor to model the experimental scattering data.

It also should be noted, that at smaller scattering angles, 2D scattering patterns are able to reveal long-range ordering of scattering objects: for example, hexagonal pattern in tangential direction. The study [27] showed that there is no long-range order in the case of SDS@2β-CD microtubes.

3.2   Microtube melting by PLM
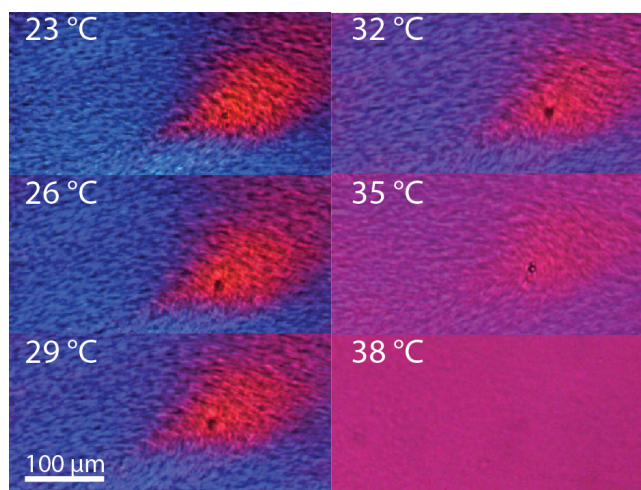
Figure 3.3: Gradual melting process for a sample of 10 wt%. Frames demonstrate a boundary between two differently oriented domains. The frames were taken as the sample was equilibrated at various temperatures in the range from room T up to T_{melting}. As temperature approaches the melting point, the contrast between domains becomes less pronounced. The sample is immobile, the domains are still present and we assume that they do not change their orientation during the heating process. We attribute the observed changes to the loss of the refractive index gradient because of disassembly of inner layers inside a tube.

Knowing that the samples consist only of microtubes, we can study their properties, for example, the melting point of the tubular phase. This goal does not require as high resolution as the SAXS technique. As microtubes are anisotropic objects, we can study them using polarized light microscopy (PLM). Two unequal light velocities propagate through anisotropic objects because of different refractive indices of the sample components. This phenomenon is called birefringence and is known to appear for the SDS@2β-CD system. PLM accompanied by the heating stage was applied to monitor the microtube melting process. A full wavelength retardation plate was used during the experiment to obtain bright, colorful images.

Figure 3.3 displays the boundary between two differently oriented domains, that are, therefore, colored differently. As the temperature increases, the refractive index gradient (Δn) becomes smaller. Eventually, at high temperatures colors of two domains become the same - birefringence disappears, anisotropic tubes are fully melted. The sample is immobile, the domains are still present and we assume that they do not change their orientation during the heating process. We attribute the gradual changes in Δn to the loss of the refractive index gradient because of disassembly of inner layers inside a tube.

This qualitative observation agrees with the study [9], where Landman *et al.* described the inward growth mechanism of the SDS@2β-CD tubes. However, to get

quantitative information on the microtube structure, methods with much higher resolution are needed.

3.3 Temperature and concentration influence: SAXS

Small-angle X-ray scattering experiments were carried out to explore the phase diagram of SDS@2β-CD microtubes. The goal of these experiments was to study how their structural features (Figure 1.4) change with the temperature.

The scales of interest in this system vary significantly: from a micron to a nanometer. This requires the exploration of a wide range of scattering angles ranging from ultra-small to wide ones. Therefore, the SAXS technique overlapping with USAXS and WAXS was used to study SDS@2β-CD microtubes.

A series of static SAXS experiments was performed for samples of different concentrations. The temperature range spanning the transition point (when the tubular phase disappears), was studied.

3.3.1 Illustrative case: 10 wt%

Static SAXS experiments: T-scans
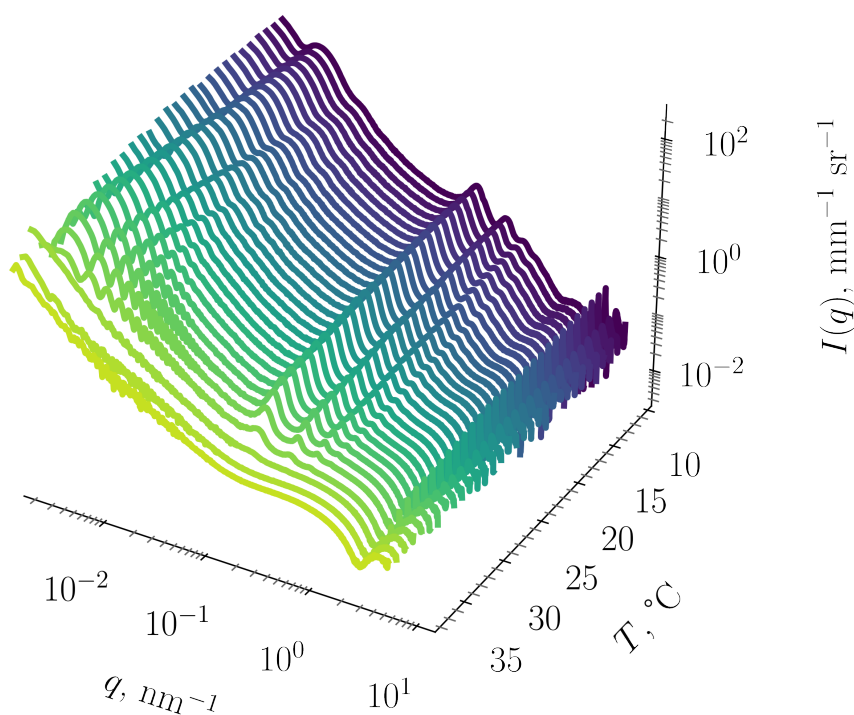
Figure 3.4: A temperature upramp series for a sample of 10 wt% concentration: the sample was slowly heated and equilibrated at each temperature from 10 to 60°C with a step of 1°C. A series of azimuthally averaged scattering curves is presented. The 3D graph makes it easier to display evolution of features inherit to the tubes at various length scales.

A temperature-dependent series of 1D SAXS patterns of a 10 wt% sample is demonstrated in Figure 3.4. These numerous patterns have been obtained by integration of normalized (by the sample transmittance) 2D patterns in azimuthal direction. Aftewards, background (water) subtraction and merging of two scattering curves recorded at different angles have been accomplished. The sample was kept long enough at each temperature to make sure that we recorded the scattering patterns of the system in equilibrium state. Referring to Figure 3.4, at low temperatures one can find vague wide oscillations in the low q region. These fingerprints display the diameter of polydisperse and dense microtubes. At higher q values there are pseudo-Bragg peaks related to the distance between cylinders inside a multiwalled tube (Equation 3.1). Because of the electron density modulation one can find higher harmonics of this peak at higher scattering vectors. Starting from 4 nm^{-1}, one can find sharp saw-tooth shaped peaks. These features result from the rhombic ordering of the complexes inside a bilayer membrane.

As temperature increases, oscillations at low q values become more pronounced. Their minimum positions shift to lower scattering vector values. This process indicates an increase in the average outermost radius. An increase in the number of oscillations refers to a more clearly defined tube size and a decrease in polydispersity. Here and below we call *transition/melting point* the temperature at which microtubes break up into separate complexes. Near this temperature, the number of oscillations at low q values increases significantly.

At the same time, lamellar peaks shift to the higher q. This indicates that the distance between inner cylinders inside a tube becomes smaller. The rhombic lattice peak positions stay the same independently of the temperature. As temperature increases, their intensity gradually decreases. At temperatures exceeding the transition temperature, all the above-described features disappear. Only a form factor of individual complexes can be detected in the scattering patterns. This pattern is clearly seen at higher temperature in Figure 3.4. It does not have any specific fingerprints except for the minimum at high q values. The nominal length of this minimum $\frac{2\pi}{q_{\min}}$ is about the single complex length (SDS@2β-CD).

Iso-scattering point
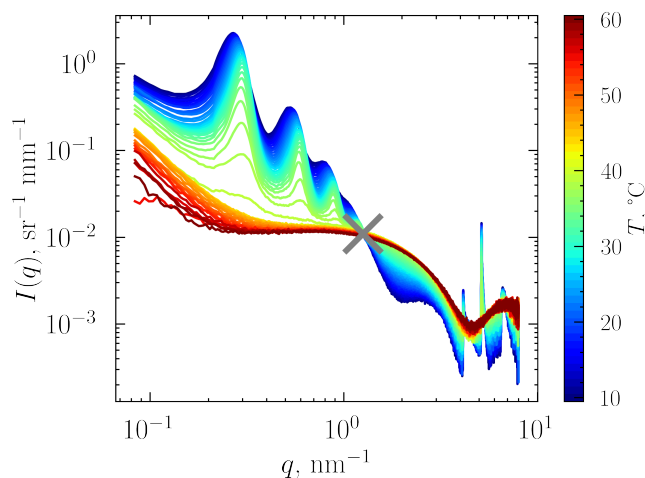
Figure 3.5: A temperature upramp series for a sample of 10 wt% concentration: zoom-in to the high-q region. A grey cross points to the iso-scaterring point (q_{iso} is around 1.25 nm^{-1}).

Let us zoom in the 3D diagram (Figure 3.4) at high q values and plot all scattering curves in $I(q)$-q coordinates. A new feature immediately catches the reader's eye in Figure 3.5: the intersection point of all curves. This point is called *iso-scattering point*. It refers to the q value for which the scattered intensity is independent of the electron density of the solvent [29]. The iso-scattering point can only occur if the objects contributing to the sample scattering in this q range transform from one scattering state to another, while the total scattering is kept constant. In this case, the total scattered intensity can be described the following way [30]:

$$I(q) = \alpha \times I_1(q) + (1 - \alpha) \times I_2(q). \tag{3.2}$$

Here, $I_1(q)$ is the scattering curve from the first scattering species multiplied by their fraction α, $I_1(q)$ - scattering from the second scattering species with a fraction $1 - \alpha$.

In Figure 3.5, a grey cross specifies the q_{iso}, where iso-scattering occurs. The presence of the q_{iso} demonstrates that the SDS@2β-CD system consists of two scattering states which pass into each other. We assume that the first scattering state is tubular aggregates (generally speaking, scattering material in a bilayer), the second one - single complexes.

To prove Equation 3.2 and search for the temperature-dependence of $\alpha(T)$, all curves were fitted in the q-range from 1.26 nm^{-1} up to 8 nm^{-1}. This q-range was chosen because at lower scattering vectors pseudo-Bragg peaks appear. As it was shown in Figure 3.4, their positions are temperature dependent. For $I_1(q)$, the scattering curve from the sample recorded at 10°C was taken, assuming that there is negligible amount of free complexes in the solution and all complexes are incorporated in tubes. $I_2(q)$ was the scattering curve taken at 50°C, when all tubes are dissolved, and scattering is mainly governed by SDS@2β-CD complexes.
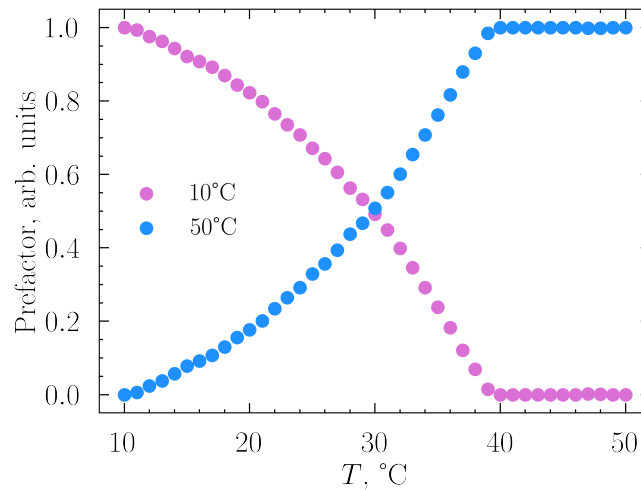
Figure 3.6: Fraction of microtubes and single complexes at different temperatures of the upramp series for a sample of 10 wt% concentration. The prefactor values have been obtained from the fitting procedure of all curves using Equation 3.2 in the q-range from 1.26 nm^{-1} up to 8 nm^{-1}.

The $\alpha(T)$ and $1 - \alpha(T)$ trends can be found in Figure 3.6. The $\alpha(T)$ behavior demonstrates that the microtube disintegration is a gradual process. The sharp change happens around 40°C, at the transition point. This observation agrees with the inward growth mechanism [9]: at temperatures lower the melting point (when

all tubes disappear), the incremental melting of inner cylindrical layers occurs. They are less energetically favourable and unstable at higher temperatures.

The similar trend is observed for Porod invariant computed for the finite q-range, available in the scattering experiment (Equation 3.7). Those results are shown in Appendix A.

3.3.2 Modelling scattering pattern

In addition to the qualitative description of the curves in Figure 3.4, quantitative information can be extracted from the recorded scattering patterns. For dilute samples (or concentrated samples with sufficient screening), interactions between objects can be neglected. This allows one to model total scattering by form factors of scatterers present in the solution.

For the azimuthally averaged SAXS profiles, the form factor of long concentric cylinders equidistantly placed inside each other can be expressed as follows:

$$I(q)_{\text{tubes}} = \frac{2\pi^2 (\Delta\rho)^2}{qR_{\text{out}}^2}$$
$$\times \sum_{m=0}^{N-1} \left(\frac{R_{\text{out}} J_1 (qR_{\text{out}})}{q} - \frac{(R_{\text{out}} - md - t_{\text{b}}) J_1 (q (R_{\text{out}} - md - t_{\text{b}}))}{q} \right)^2. \tag{3.3}$$

Here, $I(q)$ - scattered intensity, q - scattering vector, J_1 - 1st-order Bessel function, $\Delta\rho$ - difference between scattering length densities of cylindrical shells and the solvent [1], R_{out} - outermost radius of a microtube, t_{b} - bilayer thickness, N - number of cylinders inside a tube, $\langle d \rangle$ - average distance between cylindrical layers in a tube.
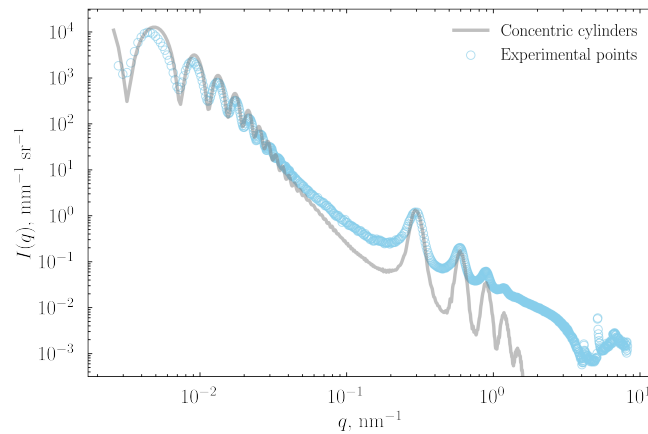
Figure 3.7: Azimuthally averaged scattering curve of the 10 wt% sample taken at 34°C (blue) and the form factor of concentric cylinders (grey).

Figure 3.7 shows a typical scattering curve fitted using the form factor of concentric cylinders (Equation 3.3). As one can see, this model decently describes oscillations in the low q region (microtube radius) and positions of pseudo-Bragg peaks related to the tube multilamellar structure. Despite the fact that the used model takes into account main structural features, the absolute intensity values are offset from the experimental data. Smearing of lamellar peaks can result from a more sophisticated form factor. For example, inner layers of a tube can freely move inside

---

[1]Calculations of the scattering length density values used to model the experimental data can be found in Appendix A.

outer layers and be not precisely concentric. This case has been considered in Appendix A. A model, taking into account other objects, that contribute to scattering was found to get better results. To fit the 1D azimuthally averaged SAXS profiles, the following model has been proposed: a linear combination of concentric cylinders and flat bilayer pieces of the size not enough to roll up and contribute to the tubular phase. The presence of the rhombus-shaped nanosheets in SDS@2β-CD solutions has been reported by Yang *et al.* [8]. To describe their contribution into the sample scattering, the form factor of infinitely thin round disks was implemented. Their scattered intensity is expressed as [31]:

$$I(q)_{\text{disk}} = \frac{8}{q^2 R^2} \left(1 - \frac{2J_1(qR)}{qR} \right),$$

(3.4)

where R - disk radius. Using the infinitely thin disk form factor is completely justified because we are interested to model intermediate q range corresponding to the length scales significantly larger than the bilayer thickness. Introduction of the nanosheet thickness ($\approx t_{\text{b}}$, 3.5 nm) is relevant for higher scattering vectors around $q = \frac{2\pi}{t_{\text{b}}} = 1.8 \text{nm}^{-1}$. For bigger length scales, such a tiny size is invisible, therefore, the simpler expression was used. The chosen disk shape (round) also does not matter as the two-dimensional nature of the scattering objects plays the major role.
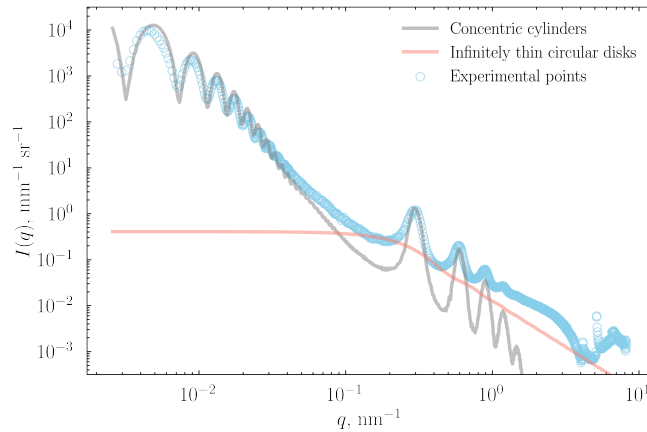
Figure 3.8: Azimuthally averaged scattering curve of the 10 wt% sample taken at 34°C (blue) and the linear combination of form factors from multiwalled tubes (grey) and disks (salmon).

The resulted fitted curve (Figure 3.8) describes the experimental data up to q range of the membrane crystal structure. It shows two contributions from the form factor of cylinders and the form factor of disks. The fitting procedure allows one to get the quantitative information on the outermost tube radius (R_{out}), the number of layers inside a tube (N), and the distance between them or interbilayer separation ($\langle d \rangle$), Figure 3.9. Of course, our system is far from perfect: Gaussian polydispersity up to 10 % was applied for parameters during the fitting procedure.

3.3.3 Concentration effect

The temperature series (as one described for 10 wt%) were recorded for samples of various concentrations: 3, 4, 5, 6.5, 7, 10, 15, 20 wt%. This allows us to study the structural temperature-dependent response as a function of concentration. In Figure 3.10 examples of the resulted fitted curves for various concentrations are shown.
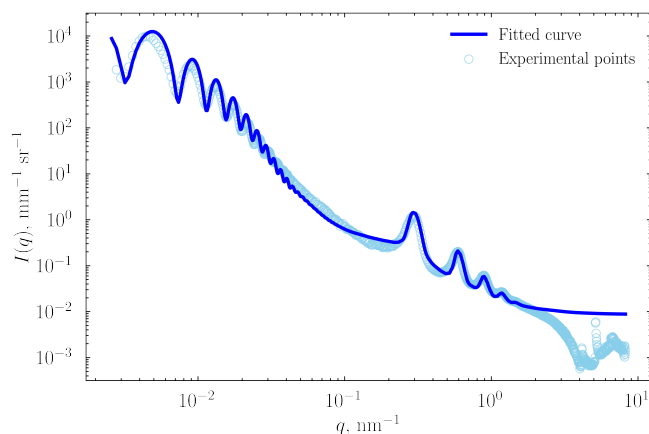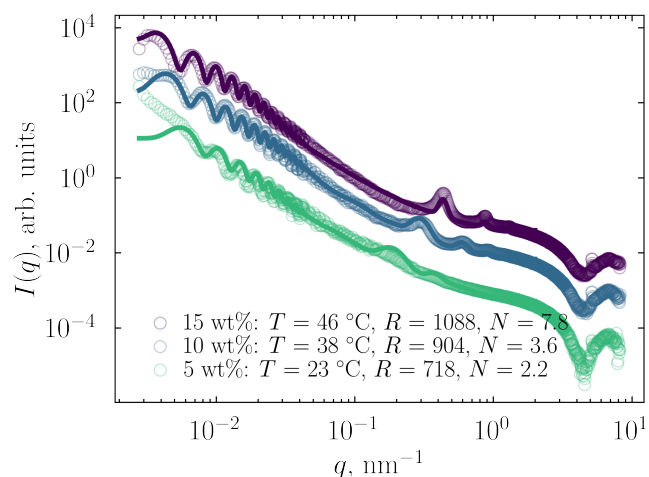
Figure 3.9: Azimuthally averaged scattering curve of the 10 wt% sample taken at 34°C (blue) and the linear combination of form factors from multiwalled tubes and disks (navy).

Qualitatively, Figure 3.10 demonstrates that for samples of high concentrations, minima at low-q oscillations are shifted to the left as the diameter of the microtubes increases.

Figure 3.10: Fitted 1D SAXS curves from the samples of various concentrations recorded at different temperatures. Circles and solid lines correspond to experimental data and fitted curves, respectively. The outermost radius values (R), the average number of cylinders in a tube (N) were extracted from the best fits. For the sake of clarity, curves are shifted at y-axis.

Lamellar peaks are shifting to the right, indicating of the more closely spaced layers. This observation is supported by the work of Landman *et al.* [9], where the inverse proportionality of the interbilayer separation from the square root of concentration in the tubular phase has been derived.

Peaks corresponding to the ordered membrane are at the same positions and have the same shape. The only difference is in the absolute intensity. Its values scale with the number of scatterers and correlate with the sample concentration.

Microtube radius

Figure 3.11 displays outermost radius values that has been found during the fitting procedure developed above. As one can see, the radius values are temperature
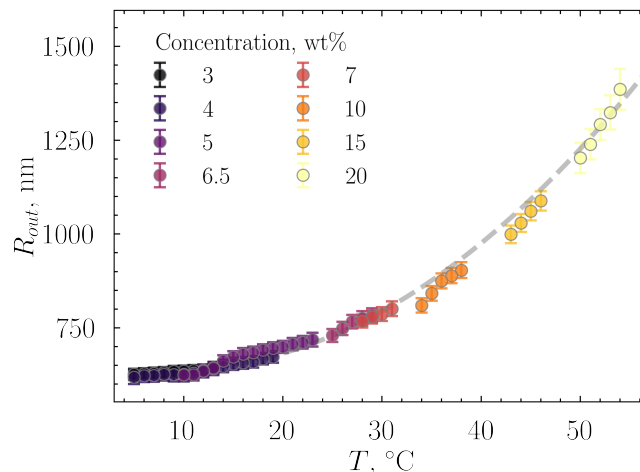
Figure 3.11: Outermost radius of microtubes for various concentrations. The values found from the fitting procedure follow the uniform temperature dependence. The grey dashed line corresponds to the parabolic fitted line with empirical parameters of the best fit result.

dependent. Peculiarly, the points are scaled with the concentration, following a uniform master curve. The grey dashed line displays a parabolic fitted line. The higher the temperature, the larger the microtube size.

According to Figure 3.11, sample concentration does not affect the microtube radius. The microtube size is almost the same at one temperature for samples with various concentrations. However, the sample concentration influences the transition temperature. Since it defines the melting point, the samples of high concentrations possess larger outermost radius values close to their transition temperature.

Near the transition point, the radius values are clearly defined for all concentrations: oscillations are pronounced and last for many orders. Beyond the transition point, at higher temperatures, all features corresponding to the multiwalled microtubes disappear.

At lower temperatures, determination of the typical size of microtubes becomes more difficult as the concentration increases. We attribute this issue to the formation of polydisperse, dense and deformed tubular structure far away from the melting point. This assumption is supported by less pronounced oscillations in the low q region and wide lamellae peaks.

Interbilayer separation

Another feature that can be tracked as a function of temperature is a distance between walls in a tube. In Figure 3.12 the interbilayer separation fluctuates near the constant value at the available temperature range for low concentrations. For samples of higher concentrations its value decreases with the temperature increase. Landman *et al.* [9] derived an expression for the interbilayer separation taking into account two contributions. Equation 3.5 relates unprofitable bending of the crystalline sheets that forces cylinders be as large as possible and electrical double-layer repulsion between charged interfaces (the membranes are negatively charged due to
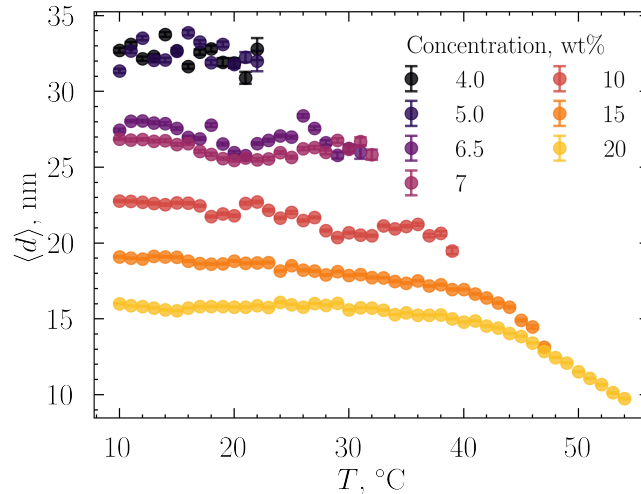
Figure 3.12: Interbilayer separation at different temperatures for various concentrations. For low concentrations, its value does not depend on the temperature and fluctuates around the average value. For higher concentrations, a certain decaying trend with the temperature increase is observed.

the SDS SO_4^- head groups). The resulted expression also takes into account temperature and concentration dependence of the interbilayer separation [2]:

$$d = \sqrt{\frac{k_B T \sigma^2}{\rho_s} \frac{4\pi R_{out}^2}{\sqrt{3}a_0 \kappa c}}. \tag{3.5}$$

As one can see, if other parameters are fixed, the interbilayer separation is inversely proportional to the square root of the concentration. The temperature term in the numerator hints at an increase in the average distance at higher temperatures. However, we observe the opposite trend in Figure 3.12: at higher temperatures, average distance between layers decreases.

The possible explanation for this dependence is the gradual disintegration of the inner, less energetically favourable, inner tube layers at high temperatures to single complexes. Free negatively charged SDS@2β-CD complexes, floating in the solution, act as salt ions. So they are contributing to the screening of the electrostatic repulsion between the cylinders inside tubes. At lower concentrations, there are no such significant changes because the samples are diluted enough not to create a crowded dense system.

Another possible explanation for this trend might be the absence of equidistant walls. Throughout the narrative, we supposed that there is equal space between all cylindrical shells. However, this space can gradually increase from the outer layers to the core of the tube. When inner shells are being melted, the contribution from larger $\langle d \rangle$-spacings is lost. Unfortunately, this reasoning is untenable in terms of energetics behind the cylindrical closure. Rolling the inner layer becomes more and more difficult, it is necessary to overcome a larger curvature. Therefore, it is more beneficial to place the innermost layers as close as possible to each other.

---

[2]In this relation, k_B is the Boltzmann constant, σ - the surface charge number density of the membrane, ρ_s - the salt number density, R_{out} - the radius of the outermost cylinder, a_0 is the interfacial area occupied by a single SDS@2β-CD complex, c - the number density of SDS@2β-CD complexes [9].

Transition temperature

With various concentrations and a wide temperature range available for studying the microtube structure (10°C - 60°C), we could restore the phase diagram of the tubular phase. This, to the best of our knowledge, was not presented elsewhere before. The system's behavior in the temperature-concentration plane is shown in Figure 3.13.

The transition temperature for every sample was defined using Porod invariant in a specific q region. In general, Porod invariant is derived from the Parseval theorem for Fourier transformations. It is computed from the scattered intensity using Equation 3.6 and tightly related to the volume irradiated in the SAXS experiment and provides the mean square electron density contrast. At different temperatures the sample is kept intact, therefore, the mean electron density contrast does not change.

$$Q = \int_0^\infty I(q)q^2 dq = 2\pi^2 \int_V \Delta\rho^2(\mathbf{r})d(\mathbf{r}). \tag{3.6}$$

The integral on the left side of Equation 3.6 taken from zero to infinity (scattering vector values) should always be constant [32]. Of course, in a real SAXS experiment, the available q-range is more modest. We can monitor changes in the mean electron density contrast between a specific scattering vector range q_{min} and q_{max}. where the scattering is governed by certain scatterers (Equation 3.7). Porod invariant changes computed in the $q_{min} - q_{max}$ region means that the number of objects scattering in this particular range is not the same. They might either agglomerate (then the scattered intensity will raise at lower q) or disintegrate to smaller constituents that scatter at higher q.

$$Q = \int_{q_{min}}^{q_{max}} I(q)q^2 dq. \tag{3.7}$$

In the case of the microtube melting, we have chosen low q values, where dominant scattering is supposed to come from tubular aggregates. Since Porod invariant is a measure of the amount of the scattering material, it should decrease as the tubes collapse and disappear (this provides with the increase in the scattered intensity at higher q values, corresponding to smaller objects). The method in detail that was used to obtain the melting point can be found in Appendix A.

In general, the higher the sample concentration, the higher its transition temperature. As has been already pointed out for the temperature series of the 10 wt% sample (Figure 3.4), at temperatures exceeding the transition point, only the form factor of single complexes is detected. The same evolution of scattering curves was found for other concentrations. Therefore, the dashed line in Figure 3.13 divides the region of the tubular phase existence and the region where only free single SDS@2β-CD complexes are present. A discrepancy between the dashed line and the outlier (4 wt%) might be due to an error in the concentration of the prepared solution, the actual concentration was higher.

A noteworthy feature of the system is the temperature range of the transition points. Figure 3.13 shows the transition point curve located near the physiological temperature. The reversible transition between tubes and single complexes around the temperature of the human body is extremely promising for controlled drug release.
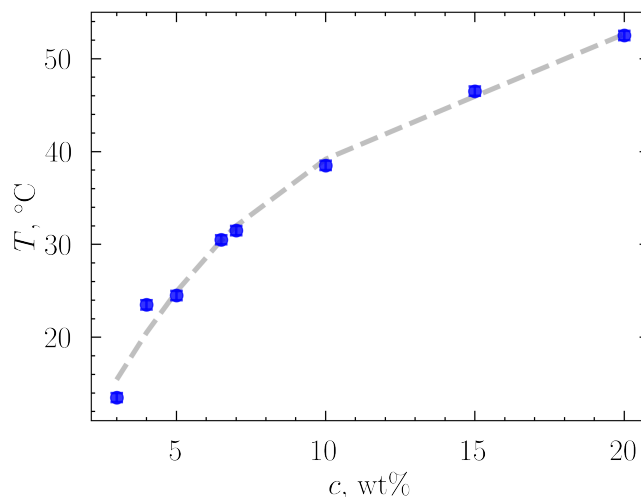
Figure 3.13: Temperature of the transition tubular phase - single SDS@2β-CD complexes for the samples of different concentrations. The grey dashed line demonstrates binodal between tubes (below) and single complexes (above).

Using temperature-dependent structural information (Figure 3.11) one can specify the size of the active substance/drugs which can fit in a tubular container. Thankfully to the extensive available temperature and concentration ranges, both radius and transition temperature values can be finely tuned by varying the initial sample concentration. β-cyclodextrin is a biocompatible cyclosaccharide, which has been extensively studying as a component of drug delivery systems [33, 34]. The replacement of sodium dodecyl sulfate with a biocompatible anionic surfactant, for example, anionic amino acid surfactants [35] can significantly expand the use of studied tubular supramolecular aggregates in real life.

Vesicles?

As one may notice, there are low-concentrated samples (3, 4, 5 wt%) present in Figure 3.13. Previously, Yang *et al.* [8] presented a phase diagram of the SDS@2β-CD system at room temperature. According to that study, at low concentrations (3-6 wt%) the complexes are self-assembled in the polyhedral phase. The presence of the polyhedra at low concentrations is also supported by the study [36] where the thermoreversible transition between tubes and capsids is observed and described.

However, the analysis of the SAXS experiment did not reveal any presence of the polyhedral objects. Even the sample of 3 wt% (the lowest available concentration) clearly shows features corresponding to the tubular phase (Figure 3.14). The significant discrepancy between the model and the experimental data is in the very low q region, which cannot be prescribed to the instrumental effect. There are several options for this mismatch. The experimental values in this range can be higher than the modeled ones because of interactions between tubes. The structure factor presence is not taken into account in this study. Another possible thing is multiple scattering: the SLD of the complex head (β-CD and the SDS sulfuric head) is around 14×10^{-4}nm^{-2}, Appendix A. For comparison, the X-ray SLD from silica nanoparticles is roughly 17×10^{-4}nm^{-2}, which drastically affects the scattering pattern from the sample at ultra-small angles [37].

In general, the temperature-dependent behavior of this sample is similar to other concentrations. At temperatures higher than the transition point, SAXS patterns do
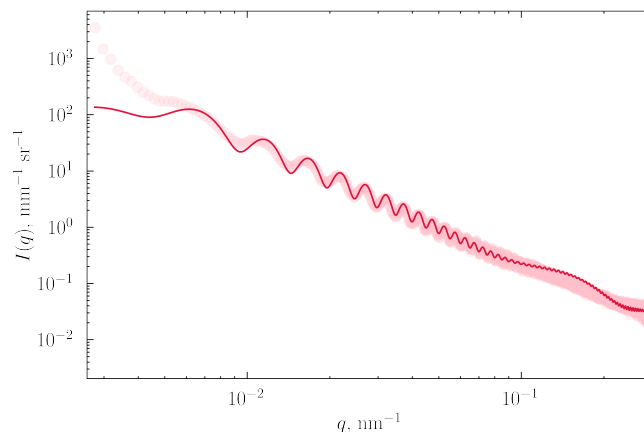
Figure 3.14: The azimuthally averaged pattern for the 3 wt% sample at 5 °C and the fitted curve - the form factor of concentric cylinders. The following fit parameters were used for the plot: R_{out} = 621 nm (polydispersity - 1.5%), $\langle d \rangle$ = 40 nm (polydispersity - 10%), N = 1.

not possess anything except for the form factor of the single complexes. Peaks at high q values, that demonstrate the presence of the crystalline membranes, disappear at the transition temperature and do not reappear after the temperature rises. There was no transition between tubes and polyhedra observed.

3.3.4 Microtube melting model

The studied static SAXS patterns do not allow us to reveal the dynamics of the transition mechanism in detail as at every temperature the system was equilibrated. Opposite, the data carries information about the system in equilibrium, which is useful for describing the balance of the forces acting on the tubes.

Previously, Landman *et al.* in their study [9] investigated the self-assembly mechanism of SDS@β-cyclodextrin complexes into micron-sized multiwalled hollow tubes using small-angle X-ray scattering. They found that the mechanism is driven by the free energy gain a crystalline bilayer of SDS@2β-CD complexes can achieve by closing into a cylinder. This happens at a very definite size given by the optimisation of free energy gain per unit interface and the penalty of bending. The result is a nucleation-dominated inward growth until a space-filling system is achieved.

In separate experiments described above we have observed the microtubes at different temperatures and different concentrations, and found that the innermost cylinders have the lowest melting temperature. Essentially, when slowly increasing the temperature of a microtube system, the tubes melt from the inside out. This is consistent with the idea that tighter wound cylinders on the inside gain less free energy by closing the cylinder because of the increased bending free energy penalty.

The two key physical parameters that determine the melting behaviour can be thought to be the bond enthalpy of a complex being incorporated into the bilayer, and the bending modulus of that bilayer. We do not have access to these parameters directly, but we can measure some key observables. While analysing the melting behaviour of the microtubes, we kept track of three key parameters: the macroscopic concentration of complexes, the temperature at which the outermost cylinder melts, and the radius of the outermost cylinder.

Connection between experiment and nanoscopic quantities

The central assumption in the model presented here is that the bond enthalpy of a complex being incorporated into a bilayer is temperature dependent, but the bending modulus, to first order, is not. We can then make use of the following relations.

The (Helmholtz) free energy of bending per unit interface of a sheet of material bent along one principal axis is given by

$$f_{\text{bend}} = \frac{\kappa}{2} \frac{1}{r^2}, \tag{3.8}$$

where κ is the elastic bending modulus of the bilayer [38] and r is the radius of the curvature. Here we have omitted the Gaussian curvature term, which is zero for all flat and cylindrical objects. Upon deforming a bilayer of width $2\pi r$ and length ℓ (assuming a roughly rectangular geometry) and closing the cylinder, the line tension along the length of the bilayer is removed. Per unit interface, the free energy gain of this process is given by

$$f_{\text{bond}} = -\frac{\tau}{2\pi} \frac{1}{r}, \tag{3.9}$$

where τ is the line tension, i.e. the free energy per unit length that arises from the unpaired bonds at the edge of the cylinder. In terms of microscopic quantities, the line tension τ scales with the typical bond energy through a length scale ℓ_0 that is on the order of the lattice parameter of the bilayer.

Summing the two contributions, and setting the derivative with respect to r to equal 0, we find an optimum cylinder radius given by

$$R_{\text{out}} = \frac{2\pi\kappa}{\tau}. \tag{3.10}$$

The optimal cylinder radius is directly experimentally accessible by measuring the SAXS pattern close to the melting temperature. Equation 3.10 fixes the ratio between κ and τ and serves as the connection between our mesoscopic observations and the molecular scale.

Single-walled cylinder melting model

We assume that at the melting point, there is an association equilibrium between a complex incorporated into a tube, and a complex floating free in solution. We consider the equilibrium

$$\text{A\,(aq)} \rightleftharpoons \text{A\,(c)} \tag{3.11}$$

The situation is somewhere between a solid-gas phase transition and a surfactant solution that can self-assemble into micelles. As such, we have the equilibrium condition

$$\mu_{\text{A}}^{(\text{aq})} = \mu_{\text{A}}^{(\text{c})}, \tag{3.12}$$

with the superscripts now denoting the aggregation state of the complex. Assuming ideal behaviour of the solution, the chemical potential of the aqueous phase can be thought to read

$$\mu_{\text{A}}^{(\text{aq})} = \mu_{\text{A}}^{\ominus(\text{aq})} + k_{\text{B}}T \log \frac{x_{\text{A}}}{x_{\text{A}}^{\ominus}}, \tag{3.13}$$

where we have chosen an arbitrary concentration to act as the reference state for which $\mu_{\text{A}}^{\ominus}$ holds. The chemical potential of a complex inside the cylinder can be seen

as the equivalent of the reference chemical potential of a pure component, $\mu_A^\star$. We then have for the equilibrium condition

$$\mu_A^\star - \mu_A^{\ominus(aq)} \equiv \Delta_r g_A = k_B T \log \frac{x_A}{x_A^\ominus}. \tag{3.14}$$

Here we have identified the difference in reference chemical potentials as the standard molar Gibbs free energy of the reaction $A\,(aq) \rightleftharpoons A\,(c)'$, which in turn can be split into an enthalpic and an entropic contribution.

$$\log \frac{x_A}{x_A^\ominus} = \frac{\Delta_r g_a}{k_B T} = \frac{\Delta_r h_A}{k_B T} + - \frac{\Delta_r s_A}{k_B}. \tag{3.15}$$

At this point the reaction can be considerably simplified by taking Equation 3.15, evaluated at the reference concentration $x_A^\ominus$,

$$\log \frac{x_A^\ominus}{x_A^\ominus} = 0 = \frac{\Delta_r h_A}{k_B T^\ominus} + - \frac{\Delta_r s_A}{k_B}, \tag{3.16}$$

and subtracting it from Equation 3.15 to cancel out the temperature independent entropy terms. We are then left with:

$$\log \frac{x_A}{x_A^\ominus} = \frac{\Delta_r h_A}{k_B} \left(\frac{1}{T} - \frac{1}{T^\ominus} \right). \tag{3.17}$$

The term in brackets can be rewritten as

$$\frac{1}{T} - \frac{1}{T^\ominus} = \frac{T^\ominus - T}{T T^\ominus} \simeq \frac{-\Delta T}{(T^\ominus)^2}, \tag{3.18}$$

where we have made use of the fact that, on the Kelvin scale, $T \approx T^\ominus$, and introduced $\Delta T = T - T^\ominus$. The resulting final expression is then

$$\log \frac{x_A}{x_A^\ominus} = \frac{-\Delta_r h_A \Delta T}{k_B (T^\ominus)^2}. \tag{3.19}$$

Connecting to the line tension

We now assume that the enthalpic contribution $\Delta_r h_A$ in Equation 3.19 is in fact the same as the bond energy gained if a complex is built into the bilayer. As such, we say that

$$\Delta_r h_A = -\frac{\ell_0 \tau}{2}, \tag{3.20}$$

where the factor $1/2$ is introduced because the structure is a bilayer. This can be inserted into Equation 3.19 to yield

$$\log \frac{x_A}{x_A^\ominus} = \frac{\ell_0 \tau \Delta T}{2 k_B (T^\ominus)^2}. \tag{3.21}$$

Of course, we do not have access to τ directly. In principle we have assumed it to be a function of temperature. However, we did find the connection earlier between the line tension τ and the experimentally accessible preferential radius R_{out}, where the bending modulus κ appears as a free parameter that is assumed to be constant over the full temperature range. In fact, we can use the fact that the line tension

plays a role in the nucleation rate, found in [9] to get an independent value for κ that provide a closure without free parameters.

For now, we insert the relationship given by Equation 3.10 into the model, yielding

$$\log \frac{x_A}{x_A^\ominus} = \frac{\pi\kappa}{k_B T^\ominus} \frac{\Delta T}{R_{out}(T)T^\ominus}. \tag{3.22}$$

In general, we expect to see the following proportionality:

$$\log \frac{x_A}{x_A^\ominus} \propto \frac{\Delta T}{R_{out}(T)}. \tag{3.23}$$

Model *vs* experiment

The derived expression was tested on the experimental data discussed above. The melting temperature, the outermost radius value in its vicinity and the sample concentration were three main parameters required to access the energetics behind the tube formation. Equation 3.23 was applied to the dataset to get the proportionality coefficient. We used different concentrations as the reference ones to obtain different slopes proportional to the bending modulus, κ. Figure 3.15 displays an example of data processing when the reference state is a 7wt% sample. Repeating the procedure for different reference concentrations, we form a sufficient sampling of the bending modulus.

.
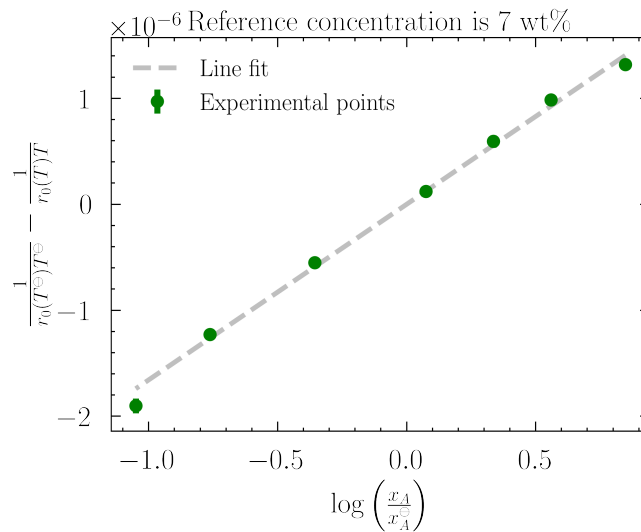
Figure 3.15: Experimental points and a linear fit following the developed model, Equation 3.22. In this figure, 7 wt% sample was used as a reference concentration $x_A^\ominus$

As it was mentioned above, SDS@2β-CD system has some similarities with natural objects: proteins, peptides [39–41]. The microtube membrane is rigid and crystalline: this is a significant difference from soft matter structures based on bilayers. Usually the bilayers are easily distorted and their bending modulus does not exceed tens of $k_B T$. Therefore, slight temperature deviations substantially affect such systems. This is not the case for SDS@2β-CD tubes.
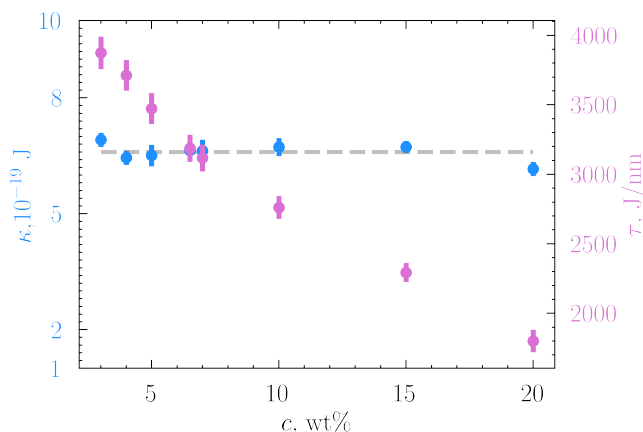
Figure 3.16: Bending modulus (blue) and line tension (pink) values obtained from the developed model. A grey dashed line demonstrates constant value of κ. The line tension decreases with the temperature increase.

Figure 3.16 demonstrates derived κ and τ values. The model assumes that bending modulus of the crystalline membrane is insensitive to the temperature and sample concentration changes considered in our experiment. It has constant values $\approx 150 k_B T$, which is extremely high. The ability to reach this quantity from the scattering experiment is amazing: usually more sophisticated methods are implemented [42]. Bending rigidity of lipid bilayer membranes is much smaller [43].

The developed model also assumed that the line tension is essentially the enthalpy contribution: its value is around $\approx 1 k_B T \text{nm}^{-1}$. According to the model, the line tension can freely change. In Figure 3.16 we see its decaying behavior as the temperature increases. This trend is typical for hydrogen-bonding in cyclodetrin aqueous solutions [44]. When temperature increases, thermal fluctuations are too high, hydrogen bonds between β-cyclodextrins are breaking and a microtube disassembles.

Despite being simple and having a few major assumptions, the presented microtube melting model gives us a decent flavor of the energies that are responsible for the microtube formation directly from the SAXS experiment. Those micro- and macroscopic values give us an idea of how to manipulate the energy of the tube formation, vary the energetic contributions. More importantly, such a model can be spread to other, completely different systems, even existing at another length scale. For example, the similar model is interesting to apply for SAXS data on carbon nanotubes. One can track conditions and geometrical parameters of their disassembly and then relate it to the energy controlling this process.

3.4 Dynamic experiments: pressure jump

Pressure is an important thermodynamic quantity that influences phase behavior of a system of interest. In particular, pressure jump affects the system's volumetric properties. Moderate pressure values (1-7 kbar) are known to affect non-covalent bonds, responsible for the formation of supramolecular aggregates. Pressure values higher 10 kbar influence covalent bonding (values are taken from the study on proteins [45]). Using the hydrostatic pressure jump provides the opportunity to study soft matter structural modifications. An instant pressure increase coupled with SAXS measurements allows one to track pressure-jump-induced kinetics of a

system in a matter of milliseconds [26]. For instance, the outlined experimental setup is widely used for studying protein folding-unfolding mechanisms [46–48]. The protein folding and unfolding processes are reversed, the protein returns back to the folded state after the pressure is released.

In a similar way, the described experimental approach was applied for SDS@2β-CD tubular aggregates to study dynamics of our system. Nuances of the experimental setup are briefly described in Chapter 2. A sample with concentration of 6.5 wt% was chosen as its melting point is near room temperature (it lies around 31°C, according to Figure 3.13.

The temperature was kept constant throughout the experiment in order to exclude the entropy contribution to the change in the energy state of the system. The experimental setup affects only the enthalpy of the system. Accompanied by SAXS, it enabled us to record the structure response related to this impact as a function of time. Modifications appearing at tiny time scales could tell us a lot about the system's dynamics.

Microtubes under pressure
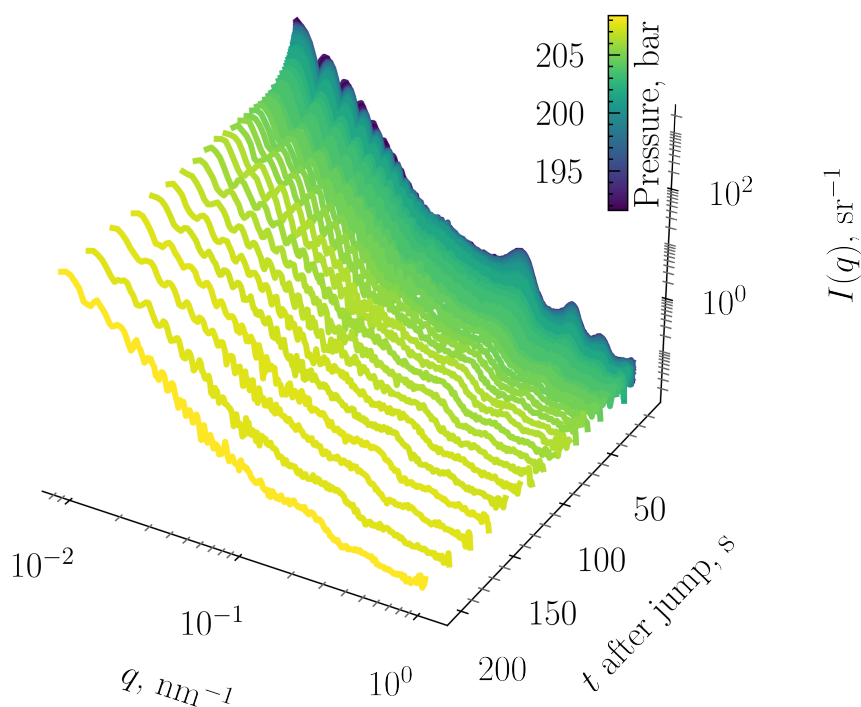
Figure 3.17: Azimuthally averaged SAXS curves of a 6.5 wt% sample after the pressure jump up to 205 bar. The curves are recorded using 10 m sample-to-detector distance. The considered q region covers oscillations related to the microtube size and pseudo-Bragg peaks from the interbilayer separation. The time intervals between the taken SAXS patterns increased in geometric progression. The positions of the minima at low q values are shifted from the very first frames. The overall scattered intensity decreases with time.

Figure 3.17 represents a 3D plot containing azimuthally averaged scattering curves of a sample subject to a pressure jump. SAXS curves were recorded at different times after the jump. The first frame was recorded before the jump. Time intervals were changing exponentially. The second frame was taken at 2 ms after the jump, the

last one after 200 s. In Figure 3.17 demonstrates the structural evolution of the microtubes. Scattering patterns cover oscillations related to the microtube diameter located at the lowest q values. They also span pseudo-Bragg peaks at higher q appeared because of the microtube multilayered organization.

Namely, the first minima at low scattering vectors shift to higher values as the sample is being compressed by $\approx$200 kbar. This displacement indicates the decrease in the typical microtube diameter. At the same time, one can notice a slight change in the interbilayer separation peaks. Those also shift to the right, pointing out on the convergence of the inner shells relative to each other. In addition, scattered intensity values drop with time resulting from the disintegration of the scatteres in the measured scattering vector range.

The chosen time range is not enough to see full disintegration of microtubes up to single complexes. Instead, shortly after the pressure jump, the changes described above occur, and after that the sample scattering pattern remains unchanged. Last five time frames are almost indistinguishable. The system does not return to its initial state after the pressure release on the time scales in which we observed it. Contrary to the results obtained in experiments where temperature scans were studied, the pressure irreversibly damages tubes. We assume that the system is being stuck in one of the local minima on the energy landscape. More precisely, the pressure jump irreparably affects the enthalpy of the tubular phase.

Quantitative view
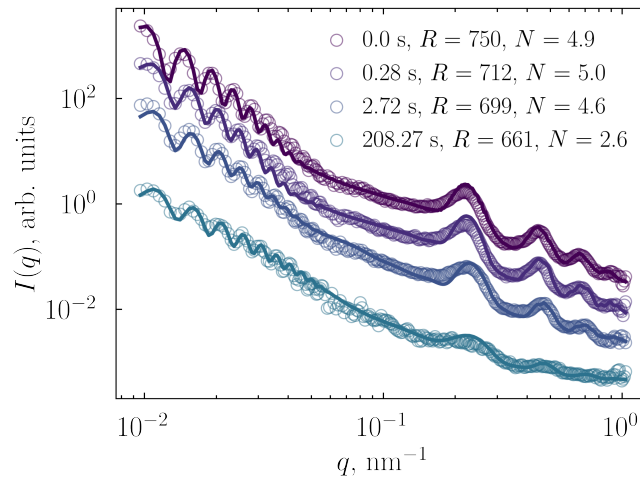
Figure 3.18: Various time frames (points) taken after the pressure jump that have been fitted using the linear combination of concentric cylinders and thin disks form factors (solid line). The legend contains a time interval when the curve was recorded, R - the outermost radius value and N the average number of cylinders in a tube from the best fit. For the sake of clarity, curves are shifted at y-axis.

Curves from Figure 3.17 were fitted using a linear combination of concentric cylinders and infinitely thin disks form factors. Similarly to Figure 3.10, several experimental curves and the best fit results are presented in Figure A.3.

Not only the microtube geometric parameters change under pressure but also the density of scattering material in the irradiated volume. The curves are placed in the figure with a constant offset. However, it is clear that the lowest curve is too far from other curves as there is a pressure-induced scattered intensity decline. Outermost radius values extracted from the fit are gradually decreases as the sample
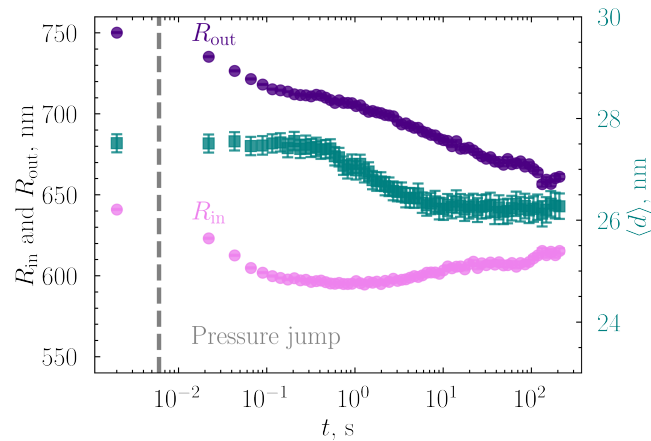
Figure 3.19: Outer and inner radius, interbilayer separation values obtained from the best fits of the recorded scattering curves. A gray dashed line separates the points before and after the jump. The data is displayed on a semi-logarithmic scale.

more and more exposed to the pressure though the number of inner layers in non-monotonous.
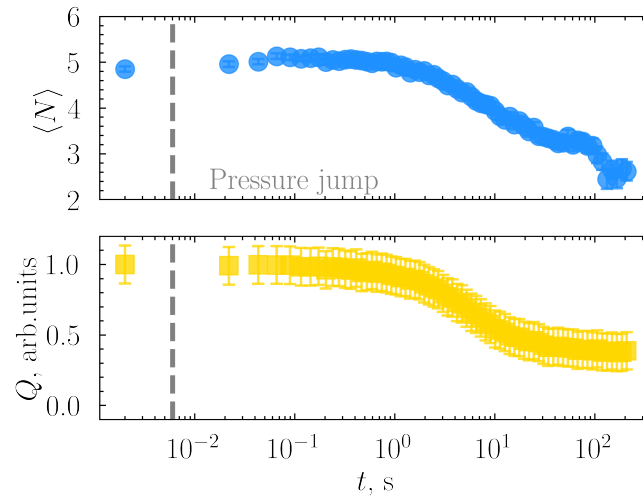
In particular, the outermost and the innermost radii, the interbilayer separation and the number of cylinders were extracted from the fitting procedure. In Figure 3.19 one can find the development of R_{out}, R_{in} and $\langle d \rangle$ with time after the jump.

Figure 3.20: The average number of cylinders inside microtubes obtained from the best fits of the recorded scattering curves (blue points). Yellow squares show "partial" Porod invariant computed using Equation 3.7 in the scattering vector region available in the SAXS experiment. A gray dashed line separates the points before and after the jump. The data is displayed on a semi-logarithmic scale.

The pink and the purple points correspond to the innermost and outermost radii, respectively. Just after the jump, both radii simultaneously decrease up to 10% with the same slope indicating microtube shrinking. Then, the outermost radius values continue declining with the same rate while the innermost radius increases. This dependence can be expressed by two processes: microtube shrinking from the outside and melting of the inner cylinders. The melting process of the inner, energetically less favourable cylindrical layers fully agrees with the inward growth mechanism of a tube formation developed by Landman *et al.* [9]. When the inner cylinder become

melted and disintegrated up to single complexes, the latter freely float in the solution. They act as ions and, therefore, contribute to the electrostatic repulsion between inner shells. Similarly to the trend that has been observed in the series with temperatures scans, the interbilayer separation becomes smaller when free complexes appear in the solution. Following Equation 3.5, the interbilayer separation decreases together with the increase in the innermost radius.

Figure 3.20 shows how the average number of cylinders inside each microtube has changed after the pressure was applied to the system. Initially, the values are slightly increasing. Accompanied by the compression in radii (Figure 3.19), these changes hint at the formation of new inner layers on account of the reduced outer ones. Then, the values follow a plateau. At the time scales larger than 1 second, inner cylinders start melting. Their disintegration is clear: the average number becomes almost two times smaller.

In addition to these parameters, Porod invariant, Q (Equation 3.7) was computed for all curves to demonstrate fluctuations in the amount of scattering material, Figure 3.20. Porod invariant is constant just after the jump but it decreases together with the number of cylinders. This process indicates the losses in a fraction of scatterers. After a significant drop, the Porod values come out on a plateau. We relate this condition with a metastable thermodynamical state.

Based on Figure 3.19 and Figure 3.20, the response of the microtube structure can be split in two processes. The first process is fast microtube shrinking around 10% in both inner and outer layers. The second process is very similar to the one we have seen analyzing temperature scans. It is mainly associated with thinning of microtubules due to melting of the inner cylindrical layers. On the contrary, the full dissasembly of microtubes was not observed. The system is being stabilized in a mixed state presumably consisting of tubes, small bilayer sheets, single SDS@2β-CD complexes.
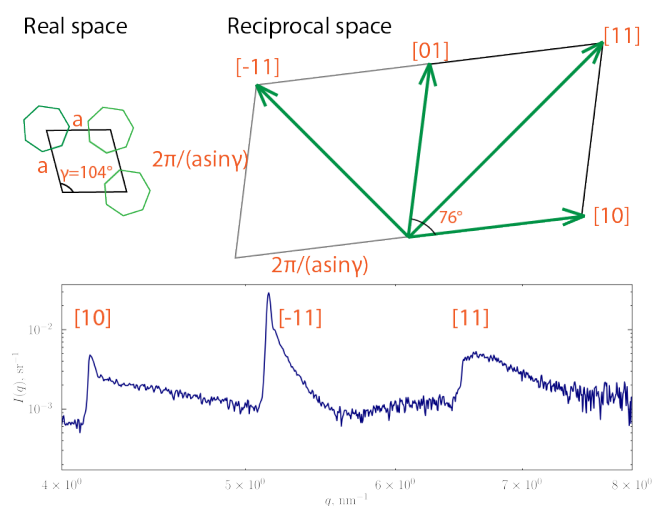
Figure 3.21: The unit cell of the membrane in real and reciprocal space. A 2D rhombic cunit cell is described by two parameters: an angle (γ) and a length (*a*). Different crystallographic directions are specified on the reciprocal unit cell as well as on the scattering pattern.

The first process, when the tubes are compressed in milliseconds after the pressure increases, is quite interesting. The simultaneous instant change in both outer and inner radii should be related with the resize in the membrane microtubes consist

of. Using smaller sample-to-detector distance, one can get the information about the pressure-induced crystalline membrane modification.

Figure 3.21 displays the 2D rhombic lattice of the bilayer membrane consists of. It is possible to track down features of the lattice in reciprocal space *via* a SAXS experiment. It contains all the necessary information about the unit cell in real space: angles and lengths. The volume of a unit cell of the reciprocal lattice is inversely proportional to the volume of the unit cell of a direct lattice. Therefore, the peak positions representing crystallographic directions provide us with information about real parameters.

In general, three crystallographic directions that might be easily monitored are [10] (or [01]), [11], [$\bar{1}$1]. The following relations between real and reciprocal space are established:

$$q_{[10]} = \frac{2\pi}{a\sin\gamma},$$

$$q_{[\bar{1}1]} = 2\sin\left(\frac{180° - \gamma}{2}\right) \times \frac{2\pi}{a\sin\gamma}, \tag{3.24}$$

$$q_{[11]} = 2\cos\left(\frac{180° - \gamma}{2}\right) \times \frac{2\pi}{a\sin\gamma}.$$

**Are there changes at smaller length scales?**

To quickly modify the microtube size, the crystalline membrane also must shrink. The mentioned compression is related to the possible changes in the parameters of the unit cell. Therefore, diffraction peak positions corresponding to the typical distances in reciprocal space also have to shift. To check if this is the case, another sample (also 6.5 wt%) was pressurized up to the similar pressure values. Scattering patterns were recorded using smaller sample-to-detector distance (1 m). The covered scattering vector range grasps diffraction peaks from the membrane lattice. If the unit cell is being deformed under pressure, shifts in the diffraction peaks can be tracked as a function of time.

Let us focus on the most intense saw-tooth shaped peak, which maximum is located at $q_{[\bar{1}1]} = 5.116\text{nm}^{-1}$. According to Figure 3.21, this peak matches the crystallographic direction [$\bar{1}$1]. Variations in the length of the unit cell a can be computed using experimental scattering vector $q_{[\bar{1}1]}$ using Equation 3.24. A distance between experimental data points (in units of the scattering vector) is defined by the pixel size of the detector in real space and the experiment geometry. The value associated with it in reciprocal space is $\Delta q = 0.006\text{nm}^{-1}$.

The peak under consideration is sharp enough and it has well-defined maximum. Therefore, we do not fit it with Gaussian or Lorentzian, but just use the experimental maximum. Assuming the lattice is compressed and the diffraction peak is being shifted to higher q values, the next data point we can measure is placed at $q_1 = q_{[\bar{1}1]} + \Delta q = 5.122\text{nm}^{-1}$. Following this, the minimal shift is possible to detect on the experimental curve depends on the q region we are interested in ($q_{[\bar{1}1]} = q_0$, the next data point $q1$) and the distance between them (Δq):

$$\delta d = \frac{2\pi}{q_0} - \frac{2\pi}{q_1} = \frac{2\pi}{q_0} - \frac{2\pi}{q_0 + \Delta q} = \frac{2\pi\Delta q}{q_0^2} = 0.0015\text{nm}. \tag{3.25}$$

Dividing this expression by the distance originating from the initial peak position ($\frac{2\pi}{q_0}$), one will find out that the scattering experiment is sensitive to the relative changes larger than $\frac{\Delta q}{q_0 + \Delta q} \times 100\%$. At given q_0 and Δq, the displacement should be
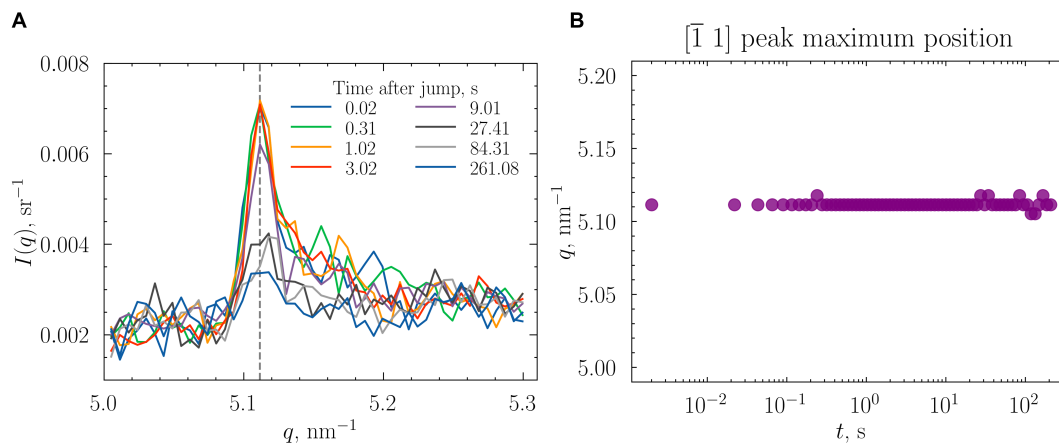
Figure 3.22: (A) A SAXS time series of a 6.5wt%-sample recorded after a pressure jump up to 180 bar using 1 m sample-to-detector distance. The curves are shown in the vicinity of the most pronounced $[\bar{1}1]$ peak from the rhombic lattice of the SDS@2β-CD membrane. The grey dashed line corresponds to the $q_{[\bar{1}1]}$ - scattering vector value corresponding to the maximum of the saw-tooth shaped peak. (B) $[\bar{1}1]$ peak maximum position $q_{[\bar{1}1]}$ tracked down over time after the jump. The measurement error is about Δq.

larger than 0.12%. Looking at the derived expression, it is easy to see that the same Δq between all data points provides better spatial resolution for larger scattering vector values, q_0.

Figure 3.22A demonstrates that the maximum position of the saw-tooth shaped peak is unaltered during the entire time-series after the jump. Only the change in the absolute intensity values can be noticed. Microtubes partially disassemble with time. As the peak area becomes smaller, it is difficult to assess whether it is still asymmetrical saw-tooth shaped or not. The grey dashed line is provided to ease the view and follow the constant peak maximum value.

According to Figure 3.19, the radius values vary up to 10%, and the membrane should also be compressed by about the same magnitude. Based on simple computations given by Equation 3.25, such shifts can be easily monitored on SAXS curves if they occur in the experiment. However, it is not the case for our system. Looking at Figure 3.22 A, one can conclude that the peak intensity gradually decreases but its position seems to be intact.

Figure 3.22B shows the maximum positions from the $[\bar{1}1]$ peak for all available time frames. The peak position does not change except for a few fluctuations supposedly resulting from low *exposure time* used in the experiment. [3] The immutable saw-tooth shaped peak position denotes that there are no changes in both reciprocal and, as a consequence, real space.

Rapid compression of a tube without any changes in its crystalline membrane may indicate a different structure of the multiwalled microtube. The simultaneous and roughly the same decrease in the inner and outer shells requires instant rearrangement of absolutely all cylindrical layers the microtube consist of. To reduce the

---

[3]Exposure time is the time interval during which a sample is examined by X-rays. With a long exposure time, radiation damage to the sample may occur. Therefore, the exposure time is adjusted before the experiment to ensure a stable scattering pattern of the sample, which would not be affected by the incoming X-ray flux.

microtube size without any manipulations with the membrane unit cell, all cylinders should become smaller by removing material, breaking the bonds between cyclodextrins. As it was estimated from the temperature scans, κ, bending modulus is relatively large and at least of the order of $150k_{\mathrm{B}}T$. Breaking hydrogen bonds and unfavorably changing the curvature of the tubes does not seem to be reasonable in the considered time scales (milliseconds). In this case, the most plausible structure of the tube is rather a long sheet rolled up in a tube with many turns inside (the turns also give rise to the pseudo-Bragg peaks) than concentric cylinders inserted into each other. When the pressure is increasing, such a roll can faster response to the compression. One would expect then to see a shift to higher q for a peak corresponding to the interbilayer separation. However, this is not the case. Again, it should be pointed out that the scattering patterns encompassing crystalline structure of the bilayer membrane (Figure 3.22B) were recorded from the different sample compared to low q oscillations displayed in Figure 3.17.

Chapter 4

Conclusions and Outlook

We have investigated the structural response of multiwalled tubular supramolecular aggregates resulting from the self-assembly of SDS@2β-CD complexes as a function of temperature and pressure. In particular, changes in outer radius values, the interbilayer separation and 2D rhombic lattice parameters were under the interest. Since the spatial scales involved in these modifications range from about a nanometer (the size of SDS@2β-CD complexes) through a micron (microtube diameter), (ultra-) small-angle X-ray scattering was proposed to be used for *in situ* in bulk experiments.

Temperature-induced microtube assembly/disassembly follows the microtube inward growth proposed by Landman et al. [9]. The outermost radius of the tubes is highly sensitive to the temperature, while SDS@2β-CD complex concentration insignificantly affects this quantity. As temperature increases towards their melting point, the number of cylinders inside a microtube decreases and the microtube swells. Temperature-dependent outer radius values follow the master curve and scale with the sample concentration. The interbilayer separation is found to be roughly independent of the temperature change for samples at lower concentrations, though for high concentrations its value decreases while approaching the melting point. Supposedly, this effect results from the melting of inner layers of the microtubes at lower temperatures and release of free SDS@2β-CD complexes. The latter act as salt ions affecting electrostatic repulsion between charged cylindrical layers.

Results of the temperature scan experiments allowed us to restore a part of the system phase diagram revealing melting points of the tubular phase for samples with various concentrations. Below binodal, the SAXS curves show the features inherit to microtubes while above it only form-factor of the single complexes was identified for all samples. At sufficiently high temperatures, microtubes completely disintegrate into single SDS@2β-CD complexes. Another worth-noticing thing is the temperature range where binodal lies is around the physiological temperature. Therefore, microtubes which melting point can be finely tuned varying the sample concentration, can be used for controlled drug release.

Assuming that microtube formation results from the interplay between bending energy and bond formation, the temperature dependence of the outermost radius of microtubes sheds light on the energetics of the self-assembly, allowing us to estimate the energies of H-bonds involved in this process.

As for the pressure jump experiment, the system demonstrates a different, two-level response to the applied moderate hydrostatic pressure (100-200 bar). The first, fast process (0.3 s) involves shrinking of microtubes without any significant changes in the number of cylinders inside or the distance between them. This fast response that is not accompanied by the change in the crystalline membrane that gives rise to a question on the real structure of the microtubes. Probably it can possess rolled-up structure instead of the concentric cylindrical shells which scattering patterns

are indistinguishable between each other. In the second slower process (tens s) microtubes disintegrate as a whole, without a transition to single-walled state. This process is not reversible.

The results of this master's project, mainly exploiting small-angle X-ray scattering, raised new questions about the microtube structure. To thoroughly study the system behavior, one might want to combine experiments in the reciprocal space with ones in real space. For example, to provide a better view on the system's thermodynamics, calorimetry can be used. This method could help us to update the developed microtube melting model. Visualization methods in real space - electron microscopy with high resolution is also needed to clarify the internal structure of the tubes. However, one has to take into account our pressure jump study that revealed gentle structure of the tubular phase. Irreversible changes of the similar nature could damage tubes during the sample preparation for cryogenic electron microscopy.

Appendix A

SAXS data modelling and useful derivations

A.1 Scattering length densities in X-ray experiments

X-ray scattering length density (SLD) is a measure of scattering of X-ray radiation by electrons. SLD of a given molecule, ρ_X can be seen as a combination of electrons and should be calculated using following expression:

$$\rho_X = \frac{r_e \times \sum n_i Z_i}{V_m}. \tag{A.1}$$

Here r_e is the Thomson scattering length (2.818×10^{-6}nm), n_i is the number density of atom i, Z_i is the atomic number of atom i (number of electrons), V_m is the molecular volume. Basically, the numerator in Equation A.1 is a total number of electrons in a molecule we are interested in.

First, let us calculate the X-ray SLD of water as it was the solvent we used in all the considered experiments. Its molecular formula H_2O, meaning each water molecule consists of two hydrogen atoms and one atom of oxygen. The water molecular volume is computed as follows:

$$V_m^{H_2O} = \frac{M_m^{H_2O}}{N_A \rho^{H_2O}} = \frac{18.015\text{g/mol}}{6.022 \times 10^{23}\text{mol}^{-1} \times 0.997 \times 10^{-21}\text{g/nm}^3} = 0.03\text{nm}^3, \tag{A.2}$$

where $M_m^{H_2O}$ is the water molar mass, N_A is the Avogadro number, ρ^{H_2O} is the water density.

Therefore, the SLD of H_2O is:

$$\rho_{H_2O} = \frac{2.818 \times 10^{-6}\text{nm} \times (2 \times 1 + 1 \times 8)}{0.03\text{nm}^3} = 9.39 \times 10^{-4}\text{nm}^{-2}. \tag{A.3}$$

The SLD of any chemical composition can be determined using with the described procedure. Regarding SDS@2β-CD microtubes, we are interested to compute the scattering length density of a bilayer cylindrical shell.

To calculate the SLD of 2 β-cyclodextrin molecules hiding a sodium dodecyl sulfate tail inside them, we, first, want to compute a total number of electrons in a pocket.

$$N_{e2\beta-CD} = 2 \times (42 \times 6 + 35 \times 8 + 70 \times 1) = 1204. \tag{A.4}$$

$$N_{eSDS^-} = 16 \times 2 + 4 \times 8 + 12 \times 6 + 25 \times 1 = 64_{SO_4^-} + 97_{\text{alkyl chain}} = 161. \quad (A.5)$$

After we know number of electrons in the components, we are interested in the volume occupied by them. Similar to Equation A.2, we can find the volume occupied per β-CD molecule:

$$V_{\beta\text{-CD}} = \frac{1134\text{g/mol} \times 10^{21}\text{nm/cm}^3}{1.44\text{g/cm}^3 \times 6.022 \times 10^{23}\text{mol}^{-1}} = 1.3\text{nm}^3. \quad (A.6)$$

The SLD of a pocket consisting of two cyclodextrins and SDS's alkyl chain is around:

$$\rho_{\text{pocket}} = \frac{(1204 + 97) \times 2.818 \times 10^{-6}\text{nm}}{2 \times 1.3\text{nm}^3} = 14.1 \times 10^{-4}\text{nm}^{-2}. \quad (A.7)$$

The obtained value (Equation A.7) is extremely high. The SDS-head (SO_4^-) is known from the literature: $\rho_{SO_4^-} \approx 12.6 \times 10^{-4}\text{nm}^{-2}$ [49]. In a bilayer, the small distance between two compexes should have the same SLD as water. As we can see from these values, the electron density is not homogeneous inside the bilayer. Using the expressions derived above and geometrical information about the complexes and the bilayer, the step-wise bilayer SLD can be restored.

As we are interested to study the sample scattering occurring at hundreds of manometers, the electron density contrast between bilayers and solvent can be simplified. To fit the experimental data we used the constant SLD difference independent of the distance. In general, more precise electron density profile of the bilayer can be derived, though it is not required for low scattering vector values we are working with.

A.2 Form factor of long, randomly-oriented concentric cylinders

To derive the form factor of long multiwalled microtubes, let us first consider a form factor of rod-like particles [50]. The form factor of such anisotropic objects with a length L and a radius R is orientation-dependent and consists of parallel and perpendicular components relative to the prinipal axis of the rod (J_1 is the Bessel function of the first order):

$$P_{rod}\left(q_{\parallel}, q_{\perp}\right) = \left[\frac{J_1(q_{\perp}R)}{q_{\perp}R}\right]^2 \left[\frac{2\sin\left(q_{\parallel}\frac{L}{2}\right)}{q_{\parallel}L}\right]^2. \quad (A.8)$$

For a hollow cylinder filled with a solvent with an outer radius R_{out}, an inner radius $R_{in} = R_{\text{out}} - \Delta t$, and $\Delta\rho$ - electron density contrast ($\rho_{rod} - \rho_{solvent}$) [1], the scattering amplitude is calculated a following way:

$$A\left(\vec{q}\right) = \Delta\rho \left(V_{out} \frac{J_1\left(q_{\perp}R_{\text{out}}\right)}{q_{\perp}R_{\text{out}}} \frac{2\sin\left(q_{\parallel}\frac{L}{2}\right)}{q_{\parallel}L} - V_{in} \frac{J_1\left(q_{\perp}R_{\text{in}}\right)}{q_{\perp}R_{\text{in}}} \frac{2\sin\left(q_{\parallel}\frac{L}{2}\right)}{q_{\parallel}L}\right), \quad (A.9)$$

---

[1] Here it is assumed that the electron density contrast between the rods and the solvent is constant. However, more complex electron density profiles may be required, arising from the multitude of structural units with different scattering length densities inside scattering objects.

where V_{out} and V_{in} are volumes of the outer and the inner cylinders.

$$A(\vec{q}) = \frac{\Delta\rho\pi L}{2}\left[\frac{R_{\text{out}}J_1(q_\perp R_{\text{out}})}{q_\perp} - \frac{R_{\text{in}}J_1(q_\perp R_{\text{in}})}{q_\perp}\right]\frac{\sin\left(q_\parallel\frac{L}{2}\right)}{q_\parallel L}$$

$$= \frac{\Delta\rho\pi}{2}\left[\frac{R_{\text{out}}J_1(q_\perp R_{\text{out}})}{q_\perp} - \frac{R_{\text{in}}J_1(q_\perp R_{\text{in}})}{q_\perp}\right]\frac{\sin\left(q_\parallel\frac{L}{2}\right)}{q_\parallel}. \tag{A.10}$$

The scattered intensity is calculated as follows:

$$I(\vec{q}) = \frac{\left\langle A^2(\vec{q})\right\rangle N_{\text{scatters}}}{V_{\text{sample}}}$$

$$= \frac{(\Delta\rho)^2\pi^2}{4}\left\langle\left(\frac{R_{\text{out}}J_1(q_\perp R_{\text{out}})}{q_\perp} - \frac{R_{\text{in}}J_1(q_\perp R_{\text{in}})}{q_\perp}\right)^2\right\rangle\left\langle\left(\frac{\sin\left(q_\parallel\frac{L}{2}\right)}{q_\parallel}\right)^2\right\rangle. \tag{A.11}$$

Since the length of the rods is much larger than their diameter ($L \gg \langle R\rangle$), the averaged square of the component in the direction parallel to the cylinder's principal axis can be simplified to the following expression:

$$\left\langle\left(\frac{\sin\left(q_\parallel\frac{L}{2}\right)}{q_\parallel}\right)^2\right\rangle = L^2\frac{2\pi}{L}\frac{\pi q}{4\pi q^2} = \frac{\pi L}{2q}. \tag{A.12}$$

With the obtained expression, scattering from one rod-like scatterer is defined by the perpendicular component:

$$I(q)_{\text{1particle}} = \frac{2\pi^3(\Delta\rho)^2 L}{q}\left(\frac{R_{\text{out}}J_1(qR_{\text{out}})}{q} - \frac{R_{\text{in}}J_1(qR_{\text{in}})}{q}\right)^2. \tag{A.13}$$

Multiplying the intensity from one particle by number density of scattering objects in the irradiated volume gives us a general expression of the cylinder form factor:

$$I(q)_{\text{Nparticles}} = \frac{2\pi^3(\Delta\rho)^2 L}{q}\frac{V_{\text{sample}}}{\pi R_{\text{out}}^2 L}\frac{1}{V_{\text{sample}}}\left(\frac{R_{\text{out}}J_1(qR_{\text{out}})}{q} - \frac{R_{\text{in}}J_1(qR_{\text{in}})}{q}\right)^2, \tag{A.14}$$

$$I(q)_{\text{Nparticles}} = \frac{2\pi^2(\Delta\rho)^2}{qR_{\text{out}}^2}\left(\frac{R_{\text{out}}J_1(qR_{\text{out}})}{q} - \frac{R_{\text{in}}J_1(qR_{\text{in}})}{q}\right)^2. \tag{A.15}$$

The multiwalled microtubes consist of a number of concentric cylinders. Therefore, the absolute intensity of the orientally averaged scattering curve will include contributions from N cylindrical shells of the thickness t_b present in the microtube [51]:

$$I(q)_{\text{Nparticles}} = \frac{2\pi^2(\Delta\rho)^2}{qR_{\text{out}}^2}\sum_{m=0}^{N-1}\left(\frac{R_{\text{out}}J_1(qR_{\text{out}})}{q}\right.$$

$$\left. - \frac{(R_{\text{out}} - md - t_b)J_1(q(R_{\text{out}} - md - t_b))}{q}\right)^2. \tag{A.16}$$

The experimental data obtained in the scattering experiment has units ster^{-1} after automatic normalization by the sample transmittance. To get the absolute scattered intensity (ster^{-1}mm^{-1}), one should also normalize the data by the sample thickness (the capillary thickness used in the experiment).

A.3 Form factor of multiwalled tubes with randomly displaced inner layers

The necessity in the new model aroused from the mismatch between the form factor of concentric cylinders (described in detail above) and the experimental intensity values. the concentric cylinders form factor describes well key fingerprints from microtube scattering: radius oscillations, interbilayer pseudo-Bragg peaks. However, there is a significant discrepancy between the model and the experimental curves. Scattered intensity is much higher in the intermediate q range near and higher 0.1 nm^{-1}. In particular, Figure 3.7 shows lamellar peaks that are significantly smeared out on the experimental curve but not on the fitted one. The scattering slope in the experiment is less steep than than the model of concentric cylinders can give.

Possible explanations of this mismatch include the presence of smaller objects that dominate the sample scattering at problematic scattering vectors. Another reason may be microtube membrane fluctuations. However, the membrane is crystalline, the so we cannot expect many degrees of freedom for it. In addition, microscopy studies on this system have shown a gigantic persistence length [8]. The third possibility is related to the microtube non-ideality. Namely, cylinders inside a tube can be not precisely concentric. They can shift relative to each other in the cross-section plane. This assumption does not contradict the electron microscopy results presented in the literature [52, 53]. However, using electron microscopy, it is difficult to determine whether such features are inherent in the structure or they appeared during sample preparation for the microscopy.

The following derivation was inspired by the study of Frielinghaus [54], where small-angle scattering from multilamellar vesicles with displaced shells was considered. Here we extended this treatment to anisotropic objects - multilayered microtubes. This form factor takes into account a possible offset of inner layers inside a tube. The form factor developed here is more computationally expensive compared with the form factor of concentric cylinders.

Assuming that the inner shells can be displaced, let us consider this movement as a random walk. First, we shold recall a single cylindrical bilayer shell scattering amplitude:

$$A(R, t_b, q) = \frac{R_{\text{out}} J_1(q R_{\text{out}})}{q} - \frac{(R_{\text{out}} - t_b) J_1(q(R_{\text{out}} - t_b))}{q}. \qquad (A.17)$$

For a multiwalled microtube consisting of N cylindrical shells, we can express a sum of the scattering amplitudes from the shells as follows:
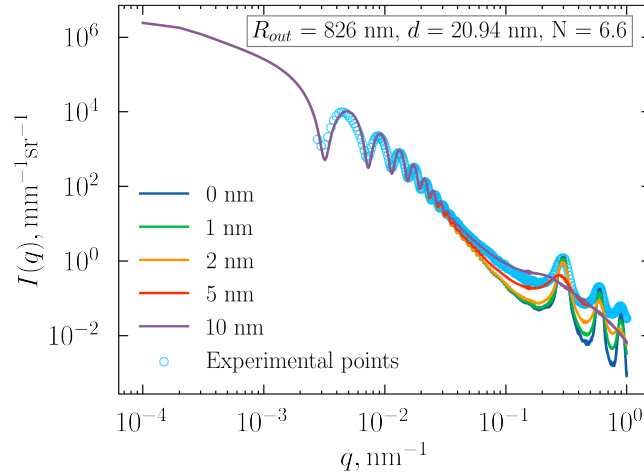
$$\sum_{m=0}^{N-1} A_m = \sum_{m=0}^{N-1} A(R_{\text{out}} - md, t_b, q) e^{iq\delta x_m}. \qquad (A.18)$$

In this expression, δx_m is the fluctuation of the position of the mth cylinder relative to the outermost cylinder with radius R_{out}.

The average intensity for Gaussian random walk:

$$\langle \sum_{m=0}^{N-1} A_m e^{imq\delta x} \times \sum_{m'=0}^{N-1} A'_m e^{-im'q\delta x} \rangle = \sum_{m=0}^{N-1} A_m \times \sum_{m'=0}^{N-1} A'_m \langle e^{-i(m'-m)q\delta x} \rangle$$

$$= \sum_{m=0}^{N-1} A_m \times \sum_{m'=0}^{N-1} A'_m K^{|m'-m|}, \qquad (A.19)$$

where $K = e^{\frac{-\sigma^2}{2}}, \sigma = \langle (q \delta x)^2 \rangle$.

Figure A.1: Experimental scattering curve (*T*-scan, 10wt%, 34^{circ}) (circles) and the modelled form factor with different average shifts inside a tube. The parameters in the upper right part of the figure were taken from the curve fit by the concentric cylinders form factor. They include outermost radius (R_{out}), interbilayer separation (*d*) values and an average number of cylinders per tube (*N*). These values were used to model scattering curves with various allowed shift values.

The resulting expression for the form factor of randomly displaced cylinders was used to model experimental data. Figure A.1 shows experimental scattering data and simulated curves with different average displacements. Because of the sterical reasons, the largest shift cannot exceed $\frac{R_{out}}{N}$. When the average shift increases, lamellar peaks of the higher orders are rapidly smeared out. The larger the displacement, the better the model at lower *q*. However, under these conditions, the interbilayer separation is not as clearly defined as for the experimental curve (Figure A.1, shift 10 nm).

Apparently there is something contributing to the electron density fluctuations at the length scales larger than the allowed shift but smaller than the microtube radius. A simulated curve that would be nicely fit the data without a significant scattering mismatch was not found in a simulation procedure (Figure A.1). Therefore, this form factor is believed to be unreasonable for our system.

A.4 Porod invariant to determine transition point

The transition temperature (where the scattering from microtubes is replaced with the scattering from the single complexes) detection can be performed using Porod invariant $Q = \int I(q)q^2 dq$ [19]. Let us consider the *q*-range (from 0.0058 nm^{-1} to 0.7 nm^{-1}) available at the SAXS experiment. In this region, features corresponding to the tubular phase for samples of all concentrations are clearly seen. At such *q* values, scattering is mostly governed by large scattering objects - microtubes. Therefore, a temperature-dependent decrease in the Porod invariant should be associated with the disappearance of these structures.

Figure Figure A.2 shows the temperature dependence of calculated Porod invariant with a downward trend that holds for all concentrations. Since the integration does not cover the q-region where scattering by single complexes takes place, we observe a decrease in scattering material. Otherwise, Porod invariant has to be constant (3.6). Melting of inner microtube shells starts from lower temperatures, so the Porod invariant becomes smaller. When all microtubes are melted, *Q* takes the constant
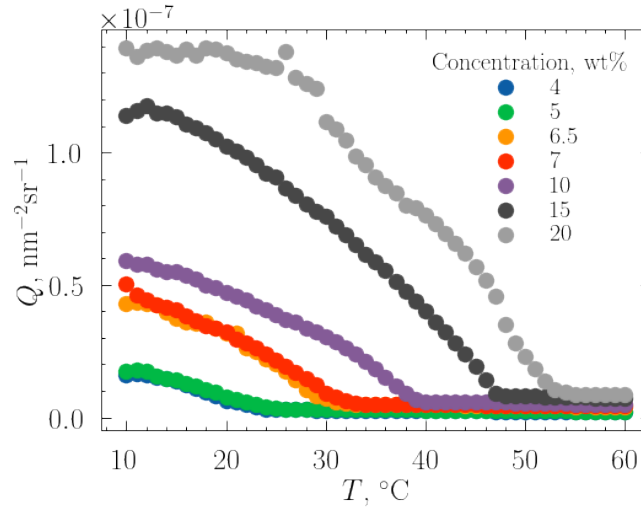
Figure A.2: Porod invariant value computed from SAXS curves for a set of concentrations and temperatures in the accessible q-region (30 m sample-to-detector distance).

minimum value, as there are no more scatters in this q-region. Using the intersection between the decaying curve and the flat line at the end, it is possible to determine the transition temperature of the sample.

From all curves in Figure Figure A.2 it is clearly seen that the melting is a gradual process, the scattering material is being lost in a wide temperature range. Assuming this decay refers to the disintegration of the inner cylinders, one can conclude its nonlinear character: at lower temperatures, only a tiny fraction of the material is lost, while at higher temperatures close to the transition, the larger fraction of the material is melted.

## A.5   Pressure-induced kinetics: useful derivation

One can consider the Gibbs energy of the system given at pressure p and temperature T in comparison with the initial state at p_0, T_0:

$$
\begin{aligned}
G\left(p,T\right) = G\left(p_0,T_0\right) - \Delta S_0\left(T-T_0\right) - \Delta C_p\langle T \log\langle\frac{T}{T_0}-1\rangle + T_0\rangle \\
+ \Delta V_0\left(p-p_0\right) + \frac{\kappa}{2}\left(p-p_0\right)^2 + \Delta\alpha\left(p-p_0\right)\left(T-T_0\right).
\end{aligned}
\tag{A.20}
$$

In the expression below, expansion in p, T is taken up to the second order. In the case of protein denaturation, pressure jump induces negative change ΔV. Temperature of the pressure-affected state is the same thanks to the small sample volume used in the experimental setup [26]. In the case of proteins, pressure jump decreases the protein volume, this process is reversible and found to be highly dependent of the solvent [4].

Below (Figure A.3) one can find the information from the pressure and temperature sensors inside a high-pressure cell. The following values have been recorded during the experiment, which results are described in Chapter 3. An instant pressure jump and minimal fluctuations observed afterwards allow one to consider stable conditions. As shown for T-scan studies in Chapter 3, microtubes are extremely sensitive to the temperature variation. Therefore, the constant temperature maintained in the pressure jump experiment (salmon curve, Figure A.3) is of crucial importance.

It shows that there was no adiabatic compression. This allows us to consider all structure modifications in this study as purely pressure-induced.
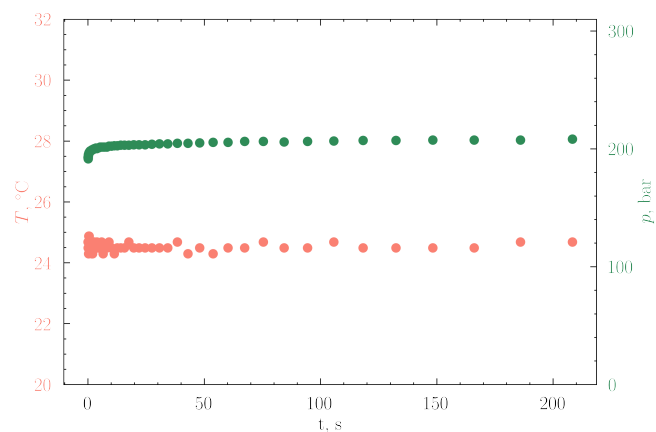
Figure A.3: Temperature and pressure values in a high-pressure cell recorded during the pressure jump experiment.

Bibliography

(1) Avvisati, G.; Dasgupta, T.; Dijkstra, M. *ACS nano* **2017**, *11*, 7702–7709.

(2) Messner, P.; Sleytr, U. B. *Advances in microbial physiology* **1992**, *33*, 213–275.

(3) Valéry, C.; Paternostre, M.; Robert, B.; Gulik-Krzywicki, T.; Narayanan, T.; Dedieu, J.-C.; Keller, G.; Torres, M.-L.; Cherif-Cheikh, R.; Calvo, P., et al. *Proceedings of the National Academy of Sciences* **2003**, *100*, 10258–10262.

(4) Kerfeld, C. A.; Sawaya, M. R.; Tanaka, S.; Nguyen, C. V.; Phillips, M.; Beeby, M.; Yeates, T. O. *Science* **2005**, *309*, 936–938.

(5) Topchieva, I.; Karezin, K. *Journal of colloid and interface science* **1999**, *213*, 29–35.

(6) Zhou, C.; Cheng, X.; Zhao, Q.; Yan, Y.; Wang, J.; Huang, J. *Langmuir* **2013**, *29*, 13175–13182.

(7) Jiang, L.; Peng, Y.; Yan, Y.; Huang, J. *Soft Matter* **2011**, *7*, 1726–1731.

(8) Yang, S.; Yan, Y.; Huang, J.; Petukhov, A. V.; Kroon-Batenburg, L. M.; Drechsler, M.; Zhou, C.; Tu, M.; Granick, S.; Jiang, L. *Nature communications* **2017**, *8*, 15856.

(9) Landman, J.; Ouhajji, S.; Prévost, S.; Narayanan, T.; Groenewold, J.; Philipse, A. P.; Kegel, W. K.; Petukhov, A. V. *Science advances* **2018**, *4*, eaat1817.

(10) Dos Santos Silva Araújo, L.; Lazzara, G.; Chiappisi, L. *Advances in Colloid and Interface Science* **2021**, *289*, 102375.

(11) Wang, K.; Jin, H.; Song, Q.; Huo, J.; Zhang, J.; Li, P. *Drug Delivery and Translational Research* **2021**, *11*, 1456–1474.

(12) Jiang, L.; de Folter, J. W.; Huang, J.; Philipse, A. P.; Kegel, W. K.; Petukhov, A. V. *Angewandte Chemie* **2013**, *125*, 3448–3452.

(13) Ouhajji, S.; Van Ravensteijn, B. G.; Fernandez-Rico, C.; Lacina, K. S.; Philipse, A. P.; Petukhov, A. V. *ACS nano* **2018**, *12*, 12089–12095.

(14) Sun, H.; Luo, Q.; Hou, C.; Liu, J. *Nano Today* **2017**, *14*, 16–41.

(15) Narayanan, T.; Konovalov, O. *Materials* **2020**, *13*, 752.

(16) Royes, J; Bjørnestad, V.; Brun, G; Narayanan, T; Lund, R; Tribet, C *Journal of Colloid and Interface Science* **2022**, *610*, 830–841.

(17) Gineste, S.; Lonetti, B.; Yon, M.; Giermanska, J.; Di Cola, E.; Sztucki, M.; Coppel, Y.; Mingotaud, A.-F.; Chapel, J.-P.; Marty, J.-D., et al. *Journal of Colloid and Interface Science* **2022**, *609*, 698–706.

(18) Narayanan, T. *Structure from diffraction methods* **2014**, 259–324.

(19) Glatter, O; Kratky, O, *Small Angle X-ray Scattering*; Academic Press: New York, 1982.

(20) Sztucki, M.; Narayanan, T. *Journal of Applied Crystallography* **2007**, *40*, 459–462.

(21) Narayanan, T.; Sztucki, M.; Van Vaerenbergh, P.; Léonardon, J.; Gorini, J.; Claustre, L.; Sever, F.; Morse, J.; Boesecke, P. *Journal of applied crystallography* **2018**, *51*, 1511–1524.

(22) Kourkoutis, L. F.; Plitzko, J. M.; Baumeister, W. *Annual review of materials research* **2012**, *42*, 33–58.

(23) Watt, J.; Huber, D. L.; Stewart, P. L. *MRS Bulletin* **2019**, *44*, 942–948.

(24) Ouhajji, S.; Landman, J.; Prévost, S.; Jiang, L.; Philipse, A. P.; Petukhov, A. V. *Soft Matter* **2017**, *13*, 2421–2425.

(25) Bilal, M; De Brauer, C.; Claudy, P; Germain, P; Létoffé, J. *Thermochimica acta* **1995**, *249*, 63–73.

(26) Möller, J.; Léonardon, J.; Gorini, J.; Dattani, R.; Narayanan, T. *Review of Scientific Instruments* **2016**, *87*, 125116.

(27) Narayanan, T.; Dattani, R.; Möller, J.; Kwaśniewski, P. *Review of Scientific Instruments* **2020**, *91*, 085102.

(28) Michael, S. **2021**, DOI: 10.5281/zenodo.5825707.

(29) Kawaguchi, T.; Hamanaka, T *Journal of applied crystallography* **1992**, *25*, 778–784.

(30) Nicolai, T; Pouzot, M; Durand, D; Weijers, M; Visschers, R. *EPL (Europhysics Letters)* **2005**, *73*, 299.

(31) Kratky, O.; Porod, G. *Journal of colloid science* **1949**, *4*, 35–70.

(32) Koch, M. H.; Vachette, P.; Svergun, D. I. *Quarterly reviews of biophysics* **2003**, *36*, 147–227.

(33) Hirayama, F; Uekama, K *Advanced drug delivery reviews* **1999**, *36*, 125–141.

(34) El-Shafai, N. M.; Masoud, M. S.; Ibrahim, M. M.; Ramadan, M. S.; Mersal, G. A.; El-Mehasseb, I. M. *International Journal of Biological Macromolecules* **2022**, *207*, 402–413.

(35) Kundu, A.; Dasmandal, S.; Majumdar, T.; Mahapatra, A. *Colloids and Surfaces A: Physicochemical and Engineering Aspects* **2013**, *419*, 216–222.

(36) Zhou, C.; Cheng, X.; Yan, Y.; Wang, J.; Huang, J. *Langmuir* **2014**, *30*, 3381–3386.

(37) Semeraro, E. F.; Möller, J.; Narayanan, T. *Journal of Applied Crystallography* **2018**, *51*, 706–713.

(38) Helfrich, W.; Servuss, R. M. *Il Nuovo Cimento D* **1984**, *3*, 137–151.

(39) Tanford, C., *The hydrophobic effect: formation of micelles and biological membranes 2d ed*; J. Wiley.: 1980.

(40) Discher, D. E.; Eisenberg, A. *Science* **2002**, *297*, 967–973.

(41) Nikolic, M. S.; Olsson, C.; Salcher, A.; Kornowski, A.; Rank, A.; Schubert, R.; Frömsdorf, A.; Weller, H.; Förster, S. *Angewandte Chemie* **2009**, *121*, 2790–2792.

(42) Dimova, R. *Advances in colloid and interface science* **2014**, *208*, 225–234.

(43) Faizi, H. A.; Frey, S. L.; Steinkühler, J.; Dimova, R.; Vlahovska, P. M. *Soft Matter* **2019**, *15*, 6006–6013.

(44) Ross, P. D.; Rekharsky, M. V. *Biophysical journal* **1996**, *71*, 2144–2154.

(45) Gilleland, G.; Lanier, T.; Hamann, D. *Journal of Food Science* **1997**, *62*, 713–733.

(46) Panick, G.; Malessa, R.; Winter, R.; Rapp, G.; Frye, K. J.; Royer, C. A. *Journal of molecular biology* **1998**, *275*, 389–402.

(47) Girard, E.; Marchal, S.; Perez, J.; Finet, S.; Kahn, R.; Fourme, R.; Marassio, G.; Dhaussy, A.-C.; Prangé, T.; Giffard, M., et al. *Biophysical journal* **2010**, *98*, 2365–2373.

(48)   Rouget, J.-B.; Schroer, M. A.; Jeworrek, C.; Pühse, M.; Saldana, J.-L.; Bessin, Y.; Tolan, M.; Barrick, D.; Winter, R.; Royer, C. A. *Biophysical Journal* **2010**, *98*, 2712–2721.

(49)   Sanchez-Fernandez, A; Edler, K. J.; Arnold, T.; Heenan, R. K.; Porcar, L.; Terrill, N. J.; Terry, A.; Jackson, A. J. *Physical Chemistry Chemical Physics* **2016**, *18*, 14063–14073.

(50)   Livsey, I. *Journal of the Chemical Society, Faraday Transactions 2* **1987**, *83*, 1445–1452.

(51)   Paineau, E.; Krapf, M.-E. M.; Amara, M.-S.; Matskova, N. V.; Dozov, I.; Rouzière, S.; Thill, A.; Launois, P.; Davidson, P. *Nature communications* **2016**, *7*, 10271.

(52)   Jiang, L.; Peng, Y.; Yan, Y.; Deng, M.; Wang, Y.; Huang, J. *Soft Matter* **2010**, *6*, 1731–1736.

(53)   Tang, X.; Chu, D.; Jiang, H.; Gong, W.; Jiang, C.; Cui, Y.; Liu, Y. *Materials Chemistry Frontiers* **2020**, *4*, 2772–2781.

(54)   Frielinghaus, H. *Physical Review E* **2007**, *76*, 051603.